The Astronomical Journal, 164:27 (30pp), 2022 July https://doi.org/10.3847/1538-3881/ac68e5

Transit Timing Variations for AU Microscopii b and c

Justin M. Wittrock[1], Stefan Dreizler[2], Michael A. Reefe[1], Brett M. Morris[3], Peter P. Plavchan[1], Patrick J. Lowrance[4], Brice-Olivier Demory[3], James G. Ingalls[4], Emily A. Gilbert[5,6,7,8,9], Thomas Barclay[6,8], Bryson L. Cale[1], Karen A. Collins[10], Kevin I. Collins[1], Ian J. M. Crossfield[11], Diana Dragomir[12], Jason D. Eastman[10], Mohammed El Mufti[1], Dax Feliz[13], Jonathan Gagné[14,15], Eric Gaidos[16], Peter Gao[17], Claire S. Geneser[18], Leslie Hebb[19], Christopher E. Henze[20], Keith D. Horne[21], Jon M. Jenkins[20], Eric L. N. Jensen[22], Stephen R. Kane[23], Laurel Kaye[24], Eder Martioli[25,26], Teresa A. Monsue[8], Enric Pallé[27,28], Elisa V. Quintana[8], Don J. Radford[29], Veronica Roccatagliata[30,31,32], Joshua E. Schlieder[8], Richard P. Schwarz[33], Avi Shporer[34], Keivan G. Stassun[13], Christopher Stockdale[35], Thiam-Guan Tan[36,37], Angelle M. Tanner[18], Andrew Vanderburg[34], Laura D. Vega[8,38,39], and Songhu Wang[40]

[1] Department of Physics & Astronomy, George Mason University, 4400 University Drive, MS 3F3, Fairfax, VA 22030, USA; jwittroc@gmu.edu
[2] Institut für Astrophysik, Georg-August-Universität, Friedrich-Hund-Platz 1, D-37077 Göttingen, Germany
[3] Center for Space and Habitability, University of Bern, Gesellschaftsstrasse 6, 3012 Bern, Switzerland
[4] IPAC-Spitzer, California Institute of Technology, MC 314-6, 1200 East California Boulevard, Pasadena, CA 91125, USA
[5] Department of Astronomy & Astrophysics, University of Chicago, 5640 South Ellis Avenue, Chicago, IL 60637, USA
[6] University of Maryland, Baltimore County, 1000 Hilltop Circle, Baltimore, MD 21250, USA
[7] The Adler Planetarium, 1300 South Lakeshore Drive, Chicago, IL 60605, USA
[8] NASA Goddard Space Flight Center, 8800 Greenbelt Road, Greenbelt, MD 20771, USA
[9] GSFC Sellers Exoplanet Environments Collaboration, USA
[10] Center for Astrophysics | Harvard & Smithsonian, 60 Garden Street, Cambridge, MA 02138, USA
[11] Department of Physics & Astronomy, University of Kansas, 1251 Wescoe Hall Drive, Lawrence, KS 66045, USA
[12] Department of Physics & Astronomy, University of New Mexico, Albuquerque, NM, USA
[13] Department of Physics & Astronomy, Vanderbilt University, 6301 Stevenson Center Lane, Nashville, TN 37235, USA
[14] Planétarium Rio Tinto Alcan, Espace pour la vie, 4801 av. Pierre-De Coubertin, Montréal, QC H1V 3V4, Canada
[15] Institute for Research on Exoplanets, Université de Montréal, Département de Physique, C.P. 6128 Succ. Centre-ville, Montréal, QC H3C 3J7, Canada
[16] University of Hawai'i at Mānoa, 1680 East-West Road, Honolulu, HI 96822, USA
[17] Earth and Planets Laboratory, Carnegie Institution for Science, 5241 Broad Branch Road NW, Washington, DC 20015, USA
[18] Mississippi State University, 75 B.S. Hood Road, Mississippi State, MS 39762, USA
[19] Physics Department, Hobart and William Smith Colleges, Geneva, NY 14456, USA
[20] NASA Ames Research Center, MS 244-30, Moffett Field, CA 94035, USA
[21] SUPA Physics and Astronomy, University of St. Andrews, Fife, KY16 9SS Scotland, UK
[22] Department of Physics & Astronomy, Swarthmore College, Swarthmore, PA 19081, USA
[23] University of California, Riverside, 900 University Avenue, Riverside, CA 92521, USA
[24] Sub-department of Astrophysics, Department of Physics, University of Oxford, Denys Wilkinson Building, Keble Road, Oxford, OX1 3RH, UK
[25] Sorbonne Université, CNRS, UMR 7095, Institut d'Astrophysique de Paris, 98 bis bd Arago, F-75014 Paris, France
[26] Laboratório Nacional de Astrofísica, Rua Estados Unidos 154, Itajubá, MG 37504-364, Brazil
[27] Instituto de Astrofísica de Canarias, Vía Láctea s/n, E-38205 La Laguna, Tenerife, Spain
[28] Departamento de Astrofísica, Universidad de La Laguna, E-38206 La Laguna, Tenerife, Spain
[29] Brierfield Observatory, Bowral, NSW, Australia
[30] Dipartimento di Fisica "Enrico Fermi", Universita' di Pisa, Largo Pontecorvo 3, I-56127 Pisa, Italy
[31] INFN, Sezione di Pisa, Largo Bruno Pontecorvo 3, I-56127 Pisa, Italy
[32] INAF–Osservatorio Astrofisico di Arcetri, Largo E. Fermi 5, I-50125 Firenze, Italy
[33] Patashnick Voorheesville Observatory, Voorheesville, NY 12186, USA
[34] Department of Physics and Kavli Institute for Astrophysics and Space Research, Massachusetts Institute of Technology, Cambridge, MA 02139, USA
[35] Hazelwood Observatory, Hazelwood South, VIC, Australia
[36] Perth Exoplanet Survey Telescope, Perth, WA, Australia
[37] Curtin Institute of Radio Astronomy, Curtin University, Bentley, 6102, WA, Australia
[38] Department of Astronomy, University of Maryland, College Park, MD 20742, USA
[39] Center for Research and Exploration in Space Science & Technology, NASA/GSFC, Greenbelt, MD 20771, USA
[40] Department of Astronomy, Indiana University, Bloomington, IN 47405, USA
Received 2021 November 10; revised 2022 March 28; accepted 2022 April 19; published 2022 June 30

Abstract

We explore the transit timing variations (TTVs) of the young (22 Myr) nearby AU Mic planetary system. For AU Mic b, we introduce three Spitzer (4.5 μm) transits, five TESS transits, 11 LCO transits, one PEST transit, one Brierfield transit, and two transit timing measurements from Rossiter–McLaughlin observations; for AU Mic c, we introduce three TESS transits. We present two independent TTV analyses. First, we use `EXOFASTv2` to jointly model the Spitzer and ground-based transits and obtain the midpoint transit times. We then construct an $O-C$ diagram and model the TTVs with `Exo-Striker`. Second, we reproduce our results with an independent photodynamical analysis. We recover a TTV mass for AU Mic c of $10.8^{+2.3}_{-2.2}$ $M_{\oplus}$. We compare the TTV-derived constraints to a recent radial velocity (RV) mass determination. We also observe excess TTVs that do not appear to

be consistent with the dynamical interactions of b and c alone or due to spots or flares. Thus, we present a hypothetical nontransiting "middle-d" candidate exoplanet that is consistent with the observed TTVs and candidate RV signal and would establish the AU Mic system as a compact resonant multiplanet chain in a 4:6:9 period commensurability. These results demonstrate that the AU Mic planetary system is dynamically interacting, producing detectable TTVs, and the implied orbital dynamics may inform the formation mechanisms for this young system. We recommend future RV and TTV observations of AU Mic b and c to further constrain the masses and confirm the existence of possible additional planet(s).

Unified Astronomy Thesaurus concepts: Exoplanets (498); Exoplanet astronomy (486)

1. Introduction

Exoplanetary science has been expanding over the past few decades, with its fields increasingly diversifying thanks in large part to several successful and diligent missions, including Kepler (Borucki et al. 2010), K2 (Howell et al. 2014), and the Transiting Exoplanet Survey Satellite (TESS; Ricker et al. 2015). TESS has detected 4548 transiting candidates (TOIs) as of 2021 October 7 and 159 confirmed planets as of 2021 October 4.[41] Many discoveries have challenged our theories of planet formation, such as hot Jupiters, e.g., 51 Pegasi b (Mayor & Queloz 1995), HD 209458 b (Henry et al. 2000), and TOI-628 b (Rodriguez et al. 2021); planets in highly eccentric orbits, e.g., 16 Cygni B b (Cochran et al. 1997), BD+63 1405 b (Dalal et al. 2021), and HD 26161 b (Rosenthal et al. 2021); and compact systems, e.g., HD 108236 (Bonfanti et al. 2021; Daylan et al. 2021), TOI-178 (Leleu et al. 2021), and TRAPPIST-1 (Gillon et al. 2016, 2017a). One way to investigate how these systems form and evolve is by probing young stellar systems when their characteristics and orbital dynamics are still undergoing progression. Several young exoplanet systems have recently been discovered by the TESS and K2 missions, e.g., DS Tucanae A (Newton et al. 2019), K2-25 (Mann et al. 2016), K2-33 (David et al. 2016), and V1298 Tauri (David et al. 2019), and other exoplanet detection methods, including direct imaging and radial velocities (RVs), e.g., HD 47366 (Sato et al. 2016), HR 8799 (Marois et al. 2008, 2010), PDS 70 (Keppler et al. 2018; Haffert et al. 2019), and βPictoris (Lagrange et al. 2009, 2019). Further probing of certain systems such as PDS 70 revealed a potentially moon-forming circumplanetary disk around PDS 70 c (Benisty et al. 2021). This new and growing population of transiting young exoplanets has recently enabled a new frontier in the study of planet formation and evolution. Among the nearby young exoplanet systems, the nearest one is AU Microscopii (Tables 1 and 2).

Object AU Microscopii (TOI-2221, TIC 441420236, HD 197481, GJ 803) is a young (22 ± 3 Myr; Mamajek & Bell 2014), nearby (9.7 pc; Bailer-Jones et al. 2018) BY Draconis variable star with spectral type M1Ve and relative brightness $m_V = 8.81$ mag. It is known to be fairly active, with numerous flares having been observed and studied at various wavelengths (Butler et al. 1981; Kundu et al. 1987; Cully et al. 1993; Tsikoudi & Kellett 2000; Gilbert et al. 2022). Kalas et al. (2004) observed the presence of a large dust disk having a radius between 50 and 210 au from the young star, having first been detected as a mid-infrared flux excess with IRAS (Fajardo-Acosta et al. 2000; Zuckerman 2001; Song et al. 2002; Liu et al. 2004; Plavchan et al. 2005). Later, Plavchan et al. (2020) discovered a Neptune-sized transiting planet, AU Mic b, interior to a spatially resolved debris disk and with an orbital period of 8.46 days. Recently, Gilbert et al. (2022) and Martioli et al. (2021) confirmed the existence of another planet, AU Mic c, with an orbital period of 18.86 days, which put the planets near a 4:9 orbital commensurability. The aforementioned traits of AU Mic and its planets make this system a unique, viable laboratory for studying the stellar activity of a young M dwarf, planetary formation, the evolution of exoplanet radii as a function of age, orbital architectures of young giant planet systems, atmospheric characteristics of young exoplanets, and the interplay between planets and disks.

One method that serves as a useful tool for probing the exoplanetary systems is transit timing variations (TTVs). Compared to other detection methods, TTVs can detect terrestrial-mass planets with greater ease (Holman & Murray 2005). The planets that are in orbital resonance with each other can amplify the TTV signals (Agol et al. 2005), so TTVs can be used to search for and measure the masses of other planets within a given stellar system (e.g., including noteworthy systems presented in Mazeh et al. 2013; Becker et al. 2015; Gillon et al. 2017a; Grimm et al. 2018). Many systems have been characterized with TTVs, such as HIP 41378 (Bryant et al. 2021), K2-146 (Lam et al. 2020), TOI-216 (Dawson et al. 2021), TOI-1266 (Demory et al. 2020), TrES-3 (Mannaday et al. 2020), and many Kepler systems (Lithwick et al. 2012; Mazeh et al. 2013; Hadden & Lithwick 2014). Martioli et al. (2021) searched for the TTVs of AU Mic transits from TESS light curves but did not identify any significant TTVs. Szabó et al. (2021) did a TTV joint model with TESS and CHEOPS data; they found AU Mic b's ~3.9 minute variation across 33 days and identifiedAU Mic c as the potential source of this perturbation. Gilbert et al. (2022) performed an independent analysis of AU Mic transits from TESS light curves and were able to detect the TTVs on the order of ~80 s.

For this paper, we examine the TTVs of AU Mic planets by incorporating additional ground and space observations into our analysis. We present the TTVs of AU Mic b and c to recover constraints on the mass for AU Mic c; the TTVs indicate the presence of TTV excess that cannot be accounted for by planets b and c alone. In Section 2, we list the light-curve data we include for TTV analysis and elaborate on some of the processes that were involved in data reduction. Section 3 covers the two critical developments: joint modeling both the ground-based photometric and Spitzer light curves and extracting the midpoint transit times from these sets using the `EXOFASTv2` package (Eastman et al. 2019), and constructing the $O - C$ diagram using the extracted midpoint times from the observations. Then, as explained in Section 4, we model the extracted TTVs using the `Exo-Striker` package (Trifonov 2019). Next, we attempt to reproduce our results with an independent and direct photodynamical analysis as described in Section 5. Lastly, we discuss the results in Section 6 and close the paper in Section 7.

[41] https://exoplanetarchive.ipac.caltech.edu

Table 1
Stellar Properties for Host Star AU Mic

Property	Unit	Quantity	References
Spectral type	⋯	M1Ve	⋯
m_V	⋯	8.81 ± 0.10	⋯
m_{TESS}	⋯	6.755 ± 0.032	⋯
α_{J2000}	h:m:s	20:45:09.53	1
δ_{J2000}	deg:arcmin:arcsec	−31:20:27.24	1
μ_α	mas yr^{-1}	281.424 ± 0.075	1
μ_δ	mas yr^{-1}	-359.895 ± 0.054	1
Distance	pc	9.7221 ± 0.0046	2
Parallax	mas	102.8295 ± 0.0486	1
$M_\star$	$M_\odot$	0.50 ± 0.03	3
$R_\star$	$R_\odot$	0.75 ± 0.03	4
$T_{\rm eff}$	K	3700 ± 100	5
$L_\star$	$L_\odot$	0.09	5
Age	Myr	22 ± 3	6
$P_{\rm rot}$	days	4.863 ± 0.010	3
$v \sin i$	km s^{-1}	8.7 ± 0.2	7

References. (1) Gaia Collaboration (2018); (2) Bailer-Jones et al. (2018); (3) Plavchan et al. (2020); (4) White et al. (2019); (5) Plavchan et al. (2009); (6) Mamajek & Bell (2014); (7) Lannier et al. (2017).

2. Data from Observations

We obtained 23 AU Mic b transits and threeAU Mic c transits from 3 yr worth of observations with multiple telescopes and included them in the analysis (Table 3). In addition to space-based observations with original transit observations from TESS and follow-ups from Spitzer, we have utilized several ground-based facilities in conducting follow-ups of AU Mic, including Brierfield, LCO SAAO, LCO SSO, and the Perth Exoplanet Survey Telescope (PEST) for photometric observations and the Canada-France-Hawai'i Telescope (CFHT) equipped with the SpectroPolarimètre InfraRouge (SPIRou), the Infrared Telescope Facility (IRTF) equipped with iSHELL, and the Very Large Telescope (VLT) equipped with the Echelle Spectrograph for Rocky Exoplanet and Stable Spectroscopic Observations (ESPRESSO) for Rossiter–McLaughlin (R-M) observations (Tables 4 and 5). The TESS transits and one of the Spitzer transits were previously presented in Plavchan et al. (2020), Gilbert et al. (2022), and Martioli et al. (2021), and the R-M observations were presented in Martioli et al. (2020) and Palle et al. (2020). The following subsections detail each telescope and the methodology employed upon their respective data sets.

2.1. TESS Photometry

TESS[42] is a space-based telescope designed to scan nearby bright F5–M5 stars for transiting exoplanets (Ricker et al. 2015). Since its launch on 2018 April 18 and the start of its primary mission on 2018 July 25, TESS has been probing the sky for ∼3 yr as of this writing and has made numerous groundbreaking contributions to planetary detection, e.g., DS Tuc A (Newton et al. 2019), TOI-700 (Gilbert et al. 2020), and TOI-1338 (Kostov et al. 2020). Its 2 yr primary mission divided the sky into the southern and northern ecliptic hemispheres, with each being divided further into 13 sectors. TESS began its search in the southern ecliptic hemisphere and probed each sector for 28 days. Within each 28 day span, a subset of primary exoplanet transit search target stars in a given sector were monitored at 2 minutes cadence, and full-frame images (FFIs) were collected at 30 minutes cadence. The data collected by TESS were then processed by the Science Processing Operations Center, which functions to generate the calibrated images, perform aperture photometry, remove systematic artifacts, and search the light curves for transiting planet signatures (Jenkins et al. 2016). TESS successfully completed its 2 yr primary mission and is now in its extended mission by repeating its observation in each of 26 sectors, with some notable differences. TESS is probing or will probe new targets along with the old targets, the 2 minute cadence for 20,000 targets per sector is boosted with a 20 s cadence for 1000 targets per sector, and FFIs are retrieved at a shorter 10 minute cadence.

TESS observed AU Mic (Figure 1) at 2 minutes cadence during Cycle 1 (Sector 1, 2018 July 25 19:00:27 UT to 2018 August 22 16:14:51 UT)[43] using Camera 1 CCD 4. This set has a 1.13 day gap due to data downlink. During its observation between 2018 August 16 16:00 UT and 2018 August 18 16:00 UT, the fine pointing mode calibration was not optimally configured, culminating in poorer data quality due to excessive spacecraft pointing jitter. Gilbert et al. (2022) employed the data quality flags to filter out the problematic part of the data set, resulting in some additional gaps in the data. TESS observed AU Mic again during Cycle 3 (Sector 27, 2020 July 5 18:31:16 UT to 2020 July 30 03:21:15 UT),[44] this time at both 20 s and 2 minute cadences, with the latter constructed by coadding six 20 s exposures. The data downlink during this period led to a 1.02 day gap in the data.

We use the AU Mic TESS Cycle 1 and 3 transit light curves from Gilbert et al. (2022) for our primary TTV analysis (Section 4), and herein we summarize their analysis. In our independent photodynamical analysis (Section 5), we reanalyze the TESS light curves directly. The AU Mic TESS Cycle 1 and 3 light curves were retrieved from the Mikulski Archive for Space Telescopes[45] using the `lightkurve` package (Lightkurve Collaboration et al. 2018) while setting its bitmask filter to "default." The Presearch Data Conditioning light curves were chosen, since they addressed crowding and instrumental systematics (Smith et al. 2012; Stumpe et al. 2012, 2014). After filtering the NaNs out of the data sets, 25.07 days of Cycle 1, 23.29 days of 2 minute Cycle 3, and 22.57 days of 20 s Cycle 3 are left. Next, the Savitzky–Golay filter is applied to the light curves to smooth out AU Mic's spot modulation. Since flares are abundant in TESS light curves, especially during most of the transits ofAU Mic b and c, the `bayesflare` (Pitkin et al. 2014) and `xoflares` packages were used to extract and model the flares instead of trimming the flares out as in Plavchan et al. (2020). Then, the `celerite2` package (Foreman-Mackey et al. 2017; Foreman-Mackey 2018) was applied to model the stellar variability of AU Mic, and the

[42] https://tess.mit.edu and https://heasarc.gsfc.nasa.gov/docs/tess.

[43] The following Guest Investigator proposals were awarded for AU Mic's Cycle 1 observations: G011176/PI Czekala, G011185/PI Davenport, G011264/PI Davenport, G011180/PI Dressing, G011239/PI Kowalski, G011175/PI Mann, and G011266/PI Schlieder.

[44] The following Guest Investigator proposals were awarded for AU Mic's Cycle 3 observations: G03272/PI Burt, G03227/PI Davenport, G03063/PI Llama, G03228/PI Million, G03205/PI Monsue, G03141/PI Newton, G03202/PI Paudel, G03263/PI Plavchan, G03226/PI Silverstein, and G03273/PI Vega.

[45] https://archive.stsci.edu

Table 2
Planetary Properties for theAU Mic System

Property	Description	Unit	AU Mic b	AU Mic c	References
$P_{\rm orb}$	Orbital period	days	$8.4630004^{+0.0000058}_{-0.0000060}$	$18.858982^{+0.000053}_{-0.000050}$	1
a	Semimajor axis	au	0.0645 ± 0.0013	0.1101 ± 0.0022	2
e	Eccentricity	⋯	$0.12^{+0.16}_{-0.08}$	$0.13^{+0.16}_{-0.09}$	1
i	Inclination	deg	89.5 ± 0.3	$89.0^{+0.5}_{-0.4}$	2
ω	Argument of periastron	deg	$-0.3^{+2.4}_{-2.3}$	$-0.3^{+2.5}_{-2.2}$	1
$M_{\rm p}$	Planetary mass	$M_{\rm J}$	0.054 ± 0.015	$0.007 < M_c < 0.079$	2
		$M_\oplus$	17 ± 5	$2 < M_c < 25$	
$R_{\rm p}$	Planetary radius	$R_{\rm J}$	$0.374^{+0.021}_{-0.020}$	$0.249^{+0.028}_{-0.027}$	1
		$R_\oplus$	$4.19^{+0.24}_{-0.22}$	$2.79^{+0.31}_{-0.30}$	
$\rho_{\rm p}$	Planetary density	g cm^{-3}	1.4 ± 0.4	$0.4 < \rho_c < 4.1$	2
K	RV semiamplitude	m s^{-1}	$8.5^{+2.3}_{-2.2}$	$0.8 < K_c < 9.5$	2
$T_{\rm C}-2{,}458{,}000$	Time of conjunction	BJD	330.39051 ± 0.00015	342.2223 ± 0.0005	2
$t_{\rm duration}$	Transit duration	hr	3.50 ± 0.08	4.5 ± 0.8	2
$R_{\rm p}/R_\star$	⋯	⋯	0.0512 ± 0.0020	$0.0340^{+0.0034}_{-0.0033}$	1
$a/R_\star$	⋯	⋯	19.1 ± 0.3	29 ± 3	2
b	Impact parameter	⋯	$0.16^{+0.13}_{-0.11}$	$0.30^{+0.21}_{-0.20}$	1

References. (1) Gilbert et al. (2022); (2) Martioli et al. (2021).

Table 3
List of AU Mic Observation Data Incorporated for TTV Analysis

Planet	Telescope	Date (UT)	Filter	Exposure Time (s)	No. of Images	Obs. Dur. (minutes)	Transit Coverage	References
b	Brierfield 0.36 m	2020-8-13	I	16	398	379	Full	⋯
b	CFHT (SPIRou)	2019-6-17	955–2515 nm	122.6	116	302.8	Egress	1
b	IRTF (iSHELL)	2019-6-17	2.18–2.47 nm	120	47	105.2	Egress	1
b	LCO SAAO 1.0 m	2020-5-20	Pan-STARRS Y	35	99	262	Egress	⋯
		2020-5-20	Pan-STARRS $z_{\rm s}$	15	333	266	Egress	
		2020-6-6	Pan-STARRS $z_{\rm s}$	15	266	218	Egress	
		2020-6-23	Pan-STARRS $z_{\rm s}$	15	223	183	Egress	
		2020-9-7	Pan-STARRS $z_{\rm s}$	15	211	172	Ingress	
		2020-10-11	Pan-STARRS $z_{\rm s}$	15	311	266	Ingress	
b	LCO SSO 1.0 m	2020-4-25	Pan-STARRS Y	35	40	104	Egress	⋯
		2020-4-25	Pan-STARRS $z_{\rm s}$	15	212	172	Egress	
		2020-8-13	Pan-STARRS $z_{\rm s}$	15	379	312	Full	
		2020-9-16	Pan-STARRS $z_{\rm s}$	15	408	340	Full	
		2020-10-3	Pan-STARRS $z_{\rm s}$	15	248	219	Egress	
b	PEST 0.30 m	2020-7-10	V	15	1143	556	Full	⋯
b	Spitzer (IRAC)	2019-2-10	4.5 μm	0.08	3020	475.7	Full	⋯
		2019-2-27	4.5 μm	0.08	3377	475.7	Egress	
		2019-9-9	4.5 μm	0.08	6002	990.9	Full	
b	TESS[b]	2018-7-26	TESS	120	329	718.0	Full	2
		2018-8-12	TESS	120	296	708.0	Full	
		2020-7-10	TESS	20	2132	719.7	Full	
		2020-7-19	TESS	20	2137	719.7	Full	
		2020-7-27	TESS	20	2120	719.7	Full	
c	TESS[b]	2018-8-11	TESS	120	342	718.0	Full	2
		2020-7-9	TESS	20	2138	719.7	Full	
		2020-7-28	TESS	20	2133	719.7	Full	
b	VLT (ESPRESSO)	2019-8-7	378.2–788.7 nm	200	88	359	Full	3

Note. All ground-based photometric observations listed here were organized via the TFOP WG.[a]
References. (1) Martioli et al. (2020); (2) Gilbert et al. (2022); (3) Palle et al. (2020).
[a] https://tess.mit.edu/followup
[b] Approximately 12 hr snippets of the ∼27 day duration TESS Cycle 1 and 3 light curves were extracted for our analysis, centered approximately on each transit.

Table 4
List of Facilities Utilized for Photometric and R-M Follow-up Observations of AU Mic

Telescope	Instrument	Location	Aperture (m)	Pixel Scale (arcsec)	Resolution (pixels)	FOV (arcmin)	References
Brierfield	Moravian 16803	Bowral, New South Wales	0.36	0.732	4096 × 4096	50 × 50	1
CFHT	SPIRou	Maunakea, Hawai'i	3.58	⋯	⋯	⋯	2
IRTF	iSHELL	Maunakea, Hawai'i	3.2	⋯	⋯	⋯	3
LCO SAAO	Sinistro	Sutherland, South Africa	1.0	0.389	4096 × 4096	26.5 × 26.5	4
LCO SSO	Sinistro	Mount Woorut, New South Wales	1.0	0.389	4096 × 4096	26.5 × 26.5	4
PEST	SBIG ST-8XME	Perth, Western Australia	0.3048	1.23	1530 × 1020	31 × 21	5
Spitzer	IRAC	⋯	0.85	1.22	256 × 256	5.2 × 5.2	6
VLT	ESPRESSO	Cerro Paranal, Chile	8.2	⋯	⋯	⋯	7

References. (1) https://www.brierfieldobservatory.com; (2) https://www.cfht.hawaii.edu; (3) http://irtfweb.ifa.hawaii.edu; (4) https://lco.global/observatory; (5) http://pestobservatory.com; (6) https://www.spitzer.caltech.edu; (7) https://www.eso.org/public/teles-instr/paranal-observatory/vlt.

Table 5
Specifications of Instruments Used for Ground-based R-M Follow-up Observations of AU Mic

Instrument	Telescope	Observing Mode	λ Range (nm)	Resolving Power	Aperture (arcsec)	Average S/N	Ref.
ESPRESSO	VLT	HR (1-UT)	378.2–788.7	140,000	1.0	93.9	1
iSHELL	IRTF	K_{gas}	2.18–2.47	75,000	0.125	65	2, 4
SPIRou	CFHT	Stokes *V* spectropolarimetric	955–2515	70,000	1.29	242	3, 4

References. (1) Donati et al. (2020); Palle et al. (2020); (2) Rayner et al. (2016); (3) Pepe et al. (2021); (4) Martioli et al. (2020).

`exoplanet` package (Foreman-Mackey et al. 2021) was utilized to model the transits of AU Mic b and c.

2.2. Spitzer (IRAC) Photometry

The Spitzer Space Telescope[46] was constructed as part of NASA's Great Observatories Program's final mission to probe various astrophysical objects at infrared wavelengths (Werner et al. 2004). Launched on 2003 August 25, Spitzer carried out its primary mission along with NASA's Astronomical Search for Origins Program for 5.75 yr, until the liquid helium coolant was depleted on 2009 May 15; afterward, it continued under several extended missions—starting with the Spitzer Warm mission, then the Spitzer Beyond mission, and finally the Spitzer Final Voyage mission—for the next 10.5 yr, from 2009 July 27 until its decommission on 2020 January 30. Spitzer fulfilled an indispensable role in characterizing exoplanets (Deming & Knutson 2020), including some benchmark systems observed, e.g., HD 189733 b (Grillmair et al. 2007; Todorov et al. 2014), HD 209458 b (Zellem et al. 2014), HD 219134 b and c (Gillon et al. 2017b), TRAPPIST-1 b through h (Ducrot et al. 2018; Morris et al. 2018; Zhang et al. 2018; Ducrot et al. 2020), and WASP-26 b (Mahtani et al. 2013).

To collect more data on the planetary object detected by TESS, Spitzer Directors Discretionary Time observations were proposed and awarded (PID 14214 and 14241) in the final year of operations for observations of AU Mic with the Infrared Array Camera (IRAC; Fazio et al. 2004) due to possible calculated transits on 2019 February 10 and 27 and September 10, which are presented in this paper. Spitzer observed AU Mic with IRAC on five occasions during the Spitzer Beyond and Final Voyage missions (2019 February 10 10:58:58–18:54:38 UT, 2019 February 27 09:46:23–17:42:02 UT, 2019 September 9 13:50:57–21:46:45 UT, 2019 September 9 23:26:02 UT to 2019 September 10 06:21:54 UT, and 2019 September 14 03:40:07–12:33:36 UT). The first two observations were originally considered to be eclipses from the initially assumed orbital period for AU Mic b from the TESS mission Cycle 1 observations. However, these observations detected additional transits of AU Mic b, establishing a true period to be half as long as originally thought (Plavchan et al. 2020). The third observation is of a transit search for an originally estimated but incorrect period for AU Mic c, and the fourth observation is of a third transit of AU Mic b; these two observations have been combined into one light-curve set for this analysis. The final observation is a secondary eclipse search of AU Mic b, which will be described and analyzed in a separate paper and is not included in this work.

All of the observations were taken using the 32 × 32 pixel subarray mode with an exposure time of 0.08 s to avoid saturation on the star (the measurement cadence is 0.1 s). After placing the star on the "sweet-spot" pixel, using the pointing calibration and reference sensor peak-up mode (Ingalls et al. 2012), we exposed with continuous staring (no dithers). The observations were all taken at 4.5 μm, as this channel has a lower systematics due to the intrapixel sensitivity. The coordinates were adjusted for the high parallax and proper motion of AU Mic for the proposed observation dates. Each observation set consisted of a 30 minute prestare dither pattern, an 8 hr stare, and a 10 minute poststare dither pattern. All data were calibrated by the Spitzer pipeline S19.2 and can be accessed using the Spitzer Heritage Archive.[47]

For each of the three transit observations discussed here, the following data reduction steps were performed on each AU Mic stellar image measured on 0.1 s intervals. We used the IDL routine `box_centroider`[48] supplied by the Spitzer Science Center to measure the location of AU Mic on the pixel. We

[46] https://www.spitzer.caltech.edu

[47] http://sha.ipac.caltech.edu

[48] https://irsa.ipac.caltech.edu/data/SPITZER/docs/irac/calibrationfiles/pixelphase/box_centroider.pro

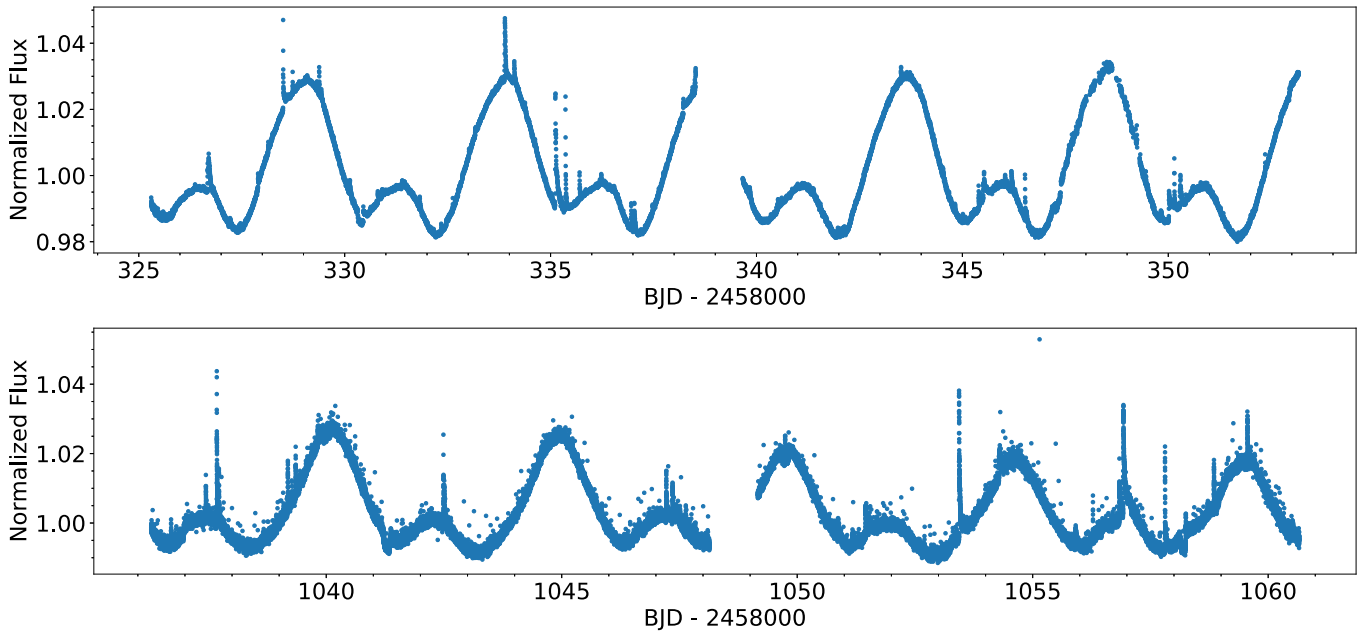

Figure 1. TESS photometry of AU Mic. The blue points are TESS measurements. The top panel is from Cycle 1 (Sector 1, 2018 July 25 19:00:27 UT to 2018 August 22 16:14:51 UT), 2 minutes cadence. The bottom panel is from Cycle 3 (Sector 27, 2020 July 05 18:31:16 UT to 2020 July 30 03:21:15 UT), 20 s cadence.

then performed aperture photometry on each image using the IDL Astronomy Users Library routine `aper`[49] with a fixed aperture of 2.25 pixels and subtracting a sky annulus of 3–7 pixels about the centroid.

All IRAC photometry at 4.5 μm contains instrumental systematics caused by the coupling between spacecraft pointing fluctuations and drifts with intrapixel sensitivity variations. For the three transit observations analyzed here, we take three approaches for detrending the instrument systematics and compare the results. First, as in Plavchan et al. (2020), we detrended this effect using an independent pixel mapping data set measured for nonvariable star BD+67 1044 (Ingalls et al. 2018). Because this calibration star does not intrinsically vary, we take its photometric variations to reflect the pixel sensitivity map. We estimated the relative pixel sensitivity at the (x, y) centroid locations of each AU Mic observation using the k-nearest neighbors with kernel regression technique described by Ingalls et al. (2018) and divided all AU Mic measurements by the sensitivities. This approach was published for the first Spitzer transit in Plavchan et al. (2020). However, we noticed that additional high-frequency (shorter than the transit duration) photometric variability remained in the light curve that looked like astrophysical "hot-spot" crossings. But we subsequently identified a strong correlation of these light-curve features with the Spitzer point-spread function (PSF) FWHM. Therefore, second, we detrend the light curve using both the trend time series for the pixel centroid motion and the PSF FWHM; this is the systematic-detrended time series that we adopt in this work for further analysis. Third, we also tested the noise-pixel technique detailed by Lewis et al. (2013) and achieved qualitatively similar results to our second approach.

We modeled the IRAC intrapixel sensitivity (Ingalls et al. 2016) using a modified implementation of the `BiLinearly-Interpolated Sub-pixel Sensitivity` (BLISS) mapping algorithm (Stevenson et al. 2012). We used a modified version of the `BLISS` mapping (BM) approach to mitigate the correlated noise associated with intrapixel sensitivity. In our photometric baseline model, we complement the BM correction with a linear function of the point-response function (PRF) FWHM. In addition to the BM, our baseline model includes the PRF's FWHM along the x- and y-axes, which significantly reduces the level of correlated noise, as shown in previous studies (e.g., Lanotte et al. 2014; Demory et al. 2016a, 2016b; Gillon et al. 2017a; Mendonça et al. 2018). Our baseline model does not include time-dependent parameters. Our implementation of this baseline model is included in a Markov Chain Monte Carlo (MCMC) framework already presented in the literature (Gillon et al. 2012). We run two chains of 200,000 steps each and check for convergence and efficient mixing using the Gelman–Rubin statistic (Gelman & Rubin 1992); all of the chains have converged with their Gelman–Rubin statistic <1.01.

We next construct a second-order polynomial model fit to account for the rotational modulation of stellar activity present in the three Spitzer light curves. With its rotational modulation of stellar activity, AU Mic is active and, on the timescale of a transit duration, can be described by a second-order polynomial (Addison et al. 2021); longer timescales would necessitate a Gaussian process (GP) or similar analysis as undertaken in Plavchan et al. (2020) and Gilbert et al. (2022) for the TESS transits. These polynomial coefficients are marginalized over in our TTV analysis to account for the timing uncertainties introduced from the rotational modulation of stellar activity. We cross-check our approach to that using a GP model in Plavchan et al. (2020) and derive consistent TTVs and corresponding uncertainties.

The second Spitzer transit also has an unusual "jump" feature during the middle of the transit that was thought to be caused by either a flare or a transit egress of another planet; we do not identify any systematic indicator that this jump coincides with. We explored the timing of AU Mic c's transits but found that none line up with Spitzer's transit of AU Mic b. So instead, we constructed and fit a custom flare model for this feature, consisting of a linear rapid rise followed by an

[49] https://idlastro.gsfc.nasa.gov/ftp/pro/idlphot/aper.pro

exponential decay. The amplitude of the flare model is marginalized over in our analysis of the TTVs to account for the impact it has on the transit times; however, the flare rise, peak, and decay times are fixed in our analysis. The adopted flare rise and decay times are informed by and consistent with the characterization of the flares in the TESS light curve analyzed in Gilbert et al. (2022). Here the second-order polynomial coefficients are degenerate with the flare times and marginalized over to account for the impact the flare has on our derived transit time and uncertainty. Since the flare did not occur during ingress or egress, it has minimal impact on our derived transit midpoint time and corresponding uncertainty.

The third Spitzer light curve was additionally detrended with an ad hoc Gaussian model given the presence of a low-level Gaussian-like trend coincident with the transit midpoint time (note that this is not a GP but rather a Gaussian change in brightness with time). Again, we do not identify a systematic indicator correlated with this brightness variation in the light curve and associate it with an astrophysical origin for AU Mic. The amplitude of the Gaussian model is marginalized over in our analysis to assess its impact on the TTVs, but the width and peak time are fixed; in this case, marginalizing over the second-order polynomial coefficients in our model again compensates for and is degenerate with any error in the fixed Gaussian centroid time and width. The astrophysical origins of this brightness change and its coincidence with the transit midpoint time, as well as other remaining residuals present in the AU Mic Spitzer light curves, as seen in Figure 2, are beyond the scope of this work and the subject of a future publication.

For all but one detrending time series, the additive coefficients were set to zero, and the multiplicative coefficients were set to 1. The exception is the flare detrending from the second Spitzer set, with the additive coefficient set to 1 and the multiplicative coefficient set to zero. Afterward, we did a joint model of the Spitzer and ground-based photometric transits using the `EXOFASTv2` package (Eastman et al. 2019). This process to extract the midpoint transit times from the Spitzer light curves is explained in more detail in Section 3.

2.3. R-M Spectroscopy

The R-M technique is an advantageous tool in detecting and characterizing transiting exoplanets, including determining their spin–orbit alignments (Ohta et al. 2005; Winn 2007; Triaud 2018). The R-M effect is observed when the planet crosses the host star during the RV observation, blocking a portion of the star's rotational signal and generating a characteristic feature on the time series RV profile (Holt 1893; McLaughlin 1924; Rossiter 1924; Ohta et al. 2005; Winn 2007). Many exoplanets have been characterized with R-Ms, including some benchmark systems, e.g., CoRoT-3 b and HD 189733 b (Triaud et al. 2009), KELT-20 b (Rainer et al. 2021), K2-232 b (Wang et al. 2021), TOI-1431 b (Stangret et al. 2021), and WASP-17 b (Anderson et al. 2010).

An R-M observation also offers an additional way in which to derive transit midpoint times independent of photometric observations, a method that has not previously been commonly used for TTV analysis because it is resource-intensive with its use of high-resolution spectrometers on large-aperture telescopes. Today, however, TESS mission candidates are relatively brighter and nearby compared to Kepler systems and more amenable to R-M observations. We include transit midpoint times derived from two R-M observations of AU Mic b's transits that were obtained at relatively important epochs shortly after the Spitzer observations and between the 2 yr gap in the TESS observations. The first was collected using the SPIRou and iSHELL instruments, and the second was collected using the ESPRESSO instrument. We retrieved the two transit midpoint times from Martioli (2020, private communication) and Pallé (2020, private communication), respectively. The following sections summarize the work done by Martioli et al. (2020) and Palle et al. (2020) on processing the respective SPIRou + iSHELL and ESPRESSO data.

2.3.1. CFHT (SPIRou) and IRTF (iSHELL) Spectroscopy

SPIRou,[50] mounted on the 3.6 m CFHT located atop Maunakea, Hawai'i, is a high-resolution, near-infrared (NIR) spectrometer that is capable of imaging in the *YJHK* bands (0.95–2.5 μm) with a resolving power of ~70,000 and equipped with a fiber-fed cryogenic high-resolution echelle spectrograph that can perform high-precision velocimetry and spectropolarimetry, which allows it to simultaneously observe the magnetic features and stellar activities of the host stars (Donati et al. 2020). The iSHELL,[51] installed on the 3.2 m NASA IRTF also located atop Maunakea, Hawai'i, is a high-resolution 1.1–5.3 μm spectrometer with a resolving power of 75,000 and was designed to replace CSHELL as an instrument with enhanced spectroscopic capabilities (Rayner et al. 2016). These qualities make SPIRou and iSHELL useful tools to carry out follow-up observations on transiting exoplanets of young, active M dwarfs (Morin et al. 2010; Afram & Berdyugina 2019), such as AU Mic.

As part of the SPIRou Legacy Survey's Work Package 2 (Donati et al. 2020), Martioli et al. (2020) observed AU Mic on 2019 June 17 10:10:56–15:13:45 UT with SPIRou set in Stokes *V* spectropolarimetric mode and captured an egress of AU Mic b. That night, 116 spectra were collected, each taken at 122.6 s exposure, with an average signal-to-noise ratio (S/N) of 242. Martioli et al. (2020) also used iSHELL set at $K_{\rm gas}$ mode for a simultaneous but shorter observation of AU Mic (2019 June 17 11:08:19–12:53:32 UT); 47 120 s spectra were collected with that instrument, with an S/N of ~60–70. The typical seeing condition was $0.''96 \pm 0.''13$; the initial and final airmasses were 2.9 and 1.8, respectively, with a minimum of 1.59; and the Moon was 99% illuminated and $40.^{\circ}3$ from the target.

Martioli et al. (2020) implemented the reduction pipeline APERO (N. J. Cook et al. 2022, in preparation) to reduce and process the SPIRou data and calculate the cross-correlation functions (CCFs). Next, the "M2_weighted_RV_-5.mas" line mask was applied to the spectra, and the lines were masked if their telluric absorption was deeper than 40%. The line mask then underwent further refinement by removing lines not present in AU Mic's Stokes *I* spectrum using the technique from Moutou et al. (2020). The CCFs were calculated from each spectral order and summed to achieve greater precision; then, the RVs were measured from the CCF by using the velocity shift's least-squares fit. The iSHELL RVs were extracted using the `pychell` pipeline and yielded consistent RVs and precision with the SPIRou RVs (Cale et al. 2019).

Next, Martioli et al. (2020) constructed the R-M model using the `emcee` MCMC package (Foreman-Mackey et al. 2013) and the stellar activity model using the approach from Donati et al.

[50] https://www.cfht.hawaii.edu/Instruments/SPIRou
[51] http://irtfweb.ifa.hawaii.edu/~ishell

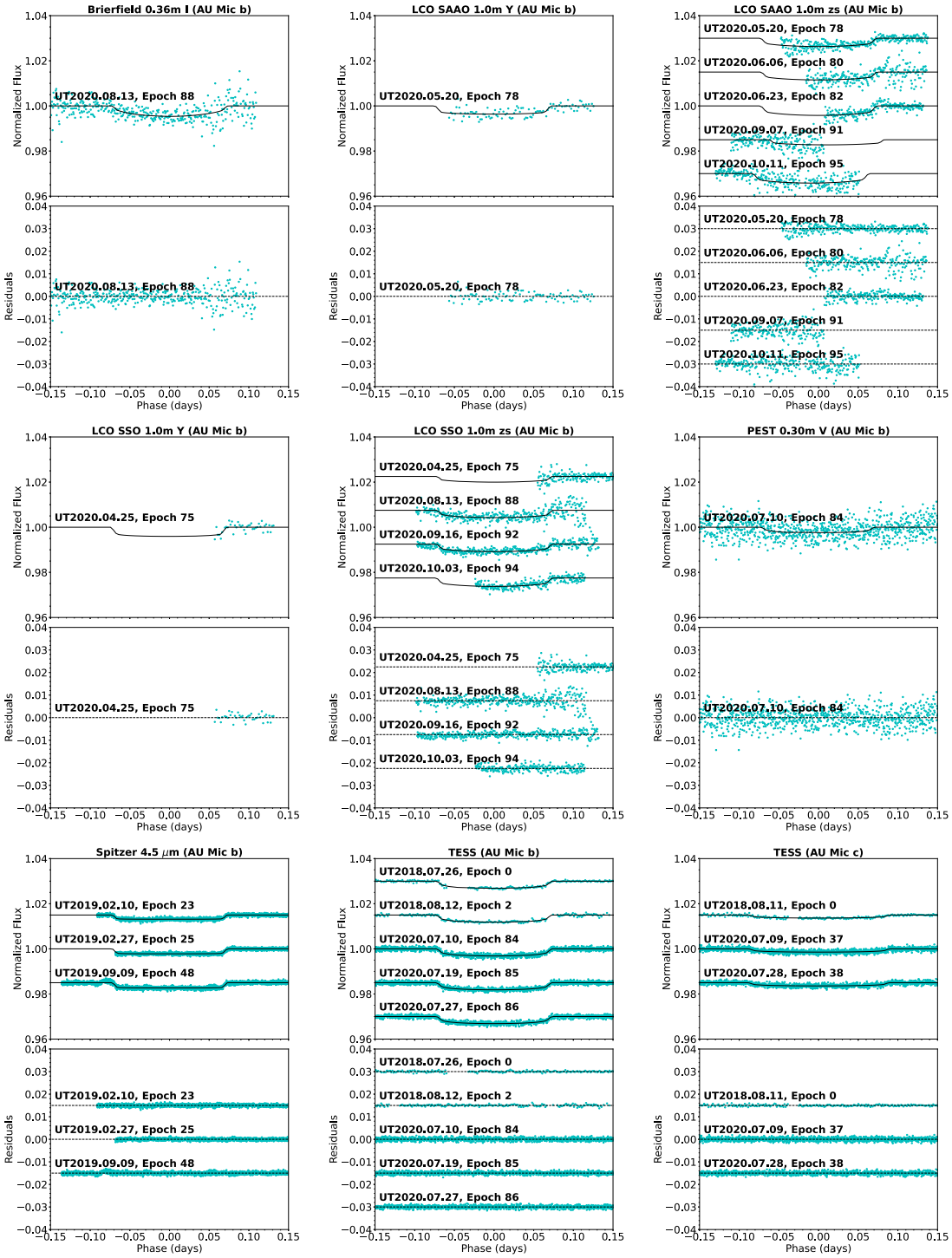

Figure 2. Two-panel plots of comparison between ground-based + Spitzer + TESS transits (cyan) and EXOFASTv2's best-fit model (black) for AU Mic b and c. The modelings are in the upper panels, and the residuals are in the lower panels. Here "epoch" refers to the number of transits since the first transit of either b or c. The Brierfield transit is obtained at epoch 88; LCO SAAO at 78, 80, 82, 91, and 95; LCO SSO at 75, 88, 92, and 94; PEST at 84; Spitzer at 23, 25, and 48; and TESS b at 0, 2, 84, 85, and 86, relative to the first TESS b transit. The TESS c transit is obtained at epochs 0, 37, and 38 relative to the first TESS c transit.

(1997). The stellar activity model was then subtracted from the measured RVs, and the R-M model was then applied as a correction to the subtracted RVs. Finally, Martioli (2020, private communication) modeled AU Mic b's midpoint time from SPIRou + iSHELL's best-fit subtracted and corrected RV model using $T_C = \mathcal{N}(2{,}458{,}330.39153,\ 0.00070)$ as a prior.

2.3.2. VLT (ESPRESSO) Spectroscopy

ESPRESSO[52] is a high-precision RV spectrometer situated in the Combined Coudé Laboratory at the focus of the VLT

[52] https://www.eso.org/sci/facilities/paranal/instruments/espresso.html

atop Cerro Paranal, Chile (Pepe et al. 2021). Its spectrograph probes the sky at 378.2–788.7 nm range, and it can use either four 8.2 m telescopes (4-UT) with a lower resolution of ∼70,000 or only one of them (1-UT) with higher resolutions of ∼140,000 in the High-Resolution (HR) mode or >190,000 in the Ultra-High-Resolution mode.

Palle et al. (2020) observed AU Mic on 2019 August 7 3:24–9:23 UT with ESPRESSO set at the standard HR (1-UT) mode and captured a full transit of AU Mic b. Eighty-eight spectra were collected that night, each taken at 200 s exposure. The S/N averaged around 93.9; the initial and final airmasses were 1.03 and 2.37, respectively, with a minimum of 1.007; and the sky was clear.

Palle et al. (2020) applied several separate approaches in reducing and modeling the ESPRESSO data; however, we only highlight one of those approaches, which provided us the midpoint time for this paper. The `SERVAL` package (Zechmeister et al. 2018) was implemented to extract and calibrate the spectra and generate the RV profile of AU Mic b. Next, the R-M effect was modeled using the combination of the `celerite` (Foreman-Mackey et al. 2017) package's GP and the `PyAstronomy` package (Czesla et al. 2019), and the stellar activity was modeled with a GP described by a Matérn 3/2 kernel implemented by `celerite`. These models are then applied as corrections to the ESPRESSO RV profile. Pallé (2020, private communication) extracted the midpoint time from the `SERVAL` GP + `PyAstronomy` best-fit RV profile using $T_C = \mathcal{N}(2{,}458{,}702.77277,\ 0.00189)$ as a prior.

2.4. Ground-based Photometry

The TESS Follow-up Observing Program (TFOP) Working Group (WG)[53] coordinated numerous ground-based follow-ups for various TOIs, including AU Mic. As a result, 13 AU Mic follow-up photometric transit observations were made using different observatories: one Brierfield 0.36 m, six LCO SAAO 1.0 m, five LCO SSO 1.0 m, and one PEST 0.30 m. The light curves from these observations are available online through ExoFOP-TESS[54] (Akeson et al. 2013). The follow-up observation schedules were conducted with the online version of the `TAPIR` package (Jensen 2013). We utilized `AstroImageJ` (`AIJ`; Collins et al. 2017) to process the ground-based light curves (except PEST, which was processed through their own pipeline) and then create a subset table containing only BJD_TDB, normalized detrended flux, flux uncertainty, and detrending columns from the ground-based light curves to prepare them for `EXOFASTv2` modeling and extraction of midpoint times (Section 3). The following subsections describe the role each telescope played in collecting and processing the light curves.

2.4.1. LCOGT (Sinistro) Photometry

We made use of two 1.0 m LCO Ritchey-Chrétien Cassegrain telescopes, both equipped with Sinistro, that are part of the Las Cumbres Observatory Global Telescope (LCOGT) network (Brown et al. 2013).[55] Two of Sinistro's filters used for AU Mic observations were Pan-STARRS *Y* and z_s, with central wavelength peaks at 1004.0 and 870.0 nm, respectively. The third filter, *B*, was used for simultaneous observation with *Y*; however, the data collected with *B* are omitted from this paper due to nondetection of AU Mic b's transits and more pronounced stellar activity in the bluer band.

Located on Mount Woorut near Coonabarabran, New South Wales, Australia, LCO SSO observed AU Mic on four separate nights (2020 April 25 16:03:03–17:49:38 UT at 35 s exposure with *Y* and 2020 April 25 16:00:47–18:52:43 UT, 2020 August 13 12:41:53–17:50:19 UT, 2020 September 16 09:12:31–14:41:47 UT, and 2020 October 3 09:17:36–12:36:33 UT at 15 s exposure with z_s). Forty images from the first night were collected with *Y*, and 212, 379, 408, and 248 images from the respective first, second, third, and fourth nights were collected with z_s. An egress was captured on the first and fourth nights, while a full transit was captured on the second and third nights.

Located in Sutherland, South Africa, LCO SAAO observed AU Mic on five separate nights (2020 May 20 22:53:29 UT to 2020 May 21 03:15:29 UT at 35 s exposure with *Y* and 2020 May 20 22:51:11 UT to 2020 May 21 03:17:38 UT, 2020 June 6 21:44:20 UT to 2020 June 7 01:22:36 UT, 2020 June 23 20:37:29 to 23:36:35 UT, 2020 September 7 21:55:46 UT to 2020 September 8 00:43:57 UT, and 2020 October 11 18:08:39 to 22:29:54 UT at 15 s exposure with z_s). Ninety-nine images from the first night were collected with *Y*, and 333, 266, 223, 211, and 311 images from the respective first, second, third, fourth, and fifth nights were collected with z_s. The second night's photometric quality was impacted by a combination of clouds and a full Moon. An egress was captured on the first through third nights, while an ingress was captured on the fourth and fifth nights.

All light curves from LCOGT were reduced and detrended with `AIJ`. For each LCOGT night, the following detrending parameters were applied: AIRMASS for UT2020-04-25 (*Y*), UT2020-05-20 (*Y* and z_s), UT2020-06-06, and UT2020-06-23; Width_T1 for UT2020-04-25 (z_s), UT2020-09-16, UT2020-10-03, and UT2020-10-11; AIRMASS + Width_T1 for UT2020-08-13; and Width_T1 + Sky/Pixel_T1 for UT2020-09-07. We also used `AIJ` to generate a subset table for each light curve.

2.4.2. PEST (SBIG ST-8XME) Photometry

PEST,[56] based in Perth, Western Australia, is a 12″ (0.3048 m) Meade LX200 Schmidt–Cassegrain Telescope that was equipped with an SBIG ST-8XME camera at the time of the AU Mic observation. PEST observed AU Mic on 2020 July 10 13:26:53–22:42:33 UT with *V* and captured a full transit; 1143 images were collected, each at 15 s exposure. The PEST light curve was reduced and processed through the `PEST` pipeline.[57] We then used `AIJ` to create a subset table that included the `PEST`-generated detrending parameters comp_flux + x_coord + y_coord + dist_center + fwhm + airmass + sky.

2.4.3. Brierfield (Moravian 16803) Photometry

The Brierfield Observatory,[58] located in Bowral, New South Wales, Australia, houses the 14″ (0.36 m) Planewave Corrected Dall-Kirkham Astrograph telescope mounted with the instrument Moravian G4-16000 KAF-16803. Brierfield observed AU Mic on 2020 August 13 11:35:21–17:54:35 UT with *I* and captured a full transit; 398 images were collected, each at 16 s exposure. The Brierfield light curve was reduced and detrended

[53] https://tess.mit.edu/followup
[54] https://exofop.ipac.caltech.edu/tess
[55] https://lco.global/observatory
[56] http://pestobservatory.com
[57] http://pestobservatory.com/the-pest-pipeline
[58] https://www.brierfieldobservatory.com

Table 6
Stellar, Planetary, and Transit Priors for EXOFASTv2 Modeling with AU Mic's Eight TESS, Three Spitzer, and 13 Ground Transits

Prior	Unit	Input	
		AU Mic b	AU Mic c
$\log_{10}\left(\frac{M_\star}{M_\odot}\right)$	...	$\mathcal{N}(-0.301, 0.026)$	
$R_\star$	$R_\odot$	$\mathcal{N}(0.75, 0.03)$	
$T_{\rm eff}$	K	$\mathcal{N}(3700, 100)$	
Age	Gyr	$\mathcal{N}(0.022, 0.003)$	
Parallax	mas	$\mathcal{N}(102.8295, 0.0486)$	
$T_{\rm C}$	BJD_TDB	$\mathcal{N}(2{,}458{,}330.39051)$	$\mathcal{N}(2{,}458{,}342.2223)$
$\log_{10}\left(\frac{\rm Period}{\rm days}\right)$	...	$\mathcal{N}(0.92752436)$	$\mathcal{N}(1.2755182)$
$R_{\rm p}/R_\star$	...	$\mathcal{N}(0.0512, 0.0020)$	$\mathcal{N}(0.0340, 0.0034)$
e	...	$\mathcal{N}(0.12, 0.16)$	$\mathcal{N}(0.13, 0.16)$
TTV offset	days	$\mathcal{U}(-0.02, 0.02)$	
Depth offset	...	$\mathcal{U}(-0.01, 0.01)$	

Note. Here $\mathcal{N}$ denotes the Gaussian priors, and $\mathcal{U}$ denotes the uniform priors. The Gaussian priors were taken from Tables 1 and 2, while the logarithmic functions were calculated. The TTV and depth offsets are arbitrary and applied as constraints to all transits.

with AIJ; the detrending parameters were Meridian_Flip + X(FITS)_T1 + Y(FITS)_T1 + tot_C_cnts. Afterward, a subset table was generated from this light curve with AIJ.

3. TESS, Spitzer, and Ground-based Photometric Joint Modeling

We use the EXOFASTv2 package (Eastman et al. 2019) to model the transits and characterize our light curves. EXOFASTv2 estimates the posterior probabilities through the MCMC to determine both the statistical significance of our ground-based and Spitzer detections and the confidence in the time of conjunction measurements to assess for the presence of detectable TTVs. Five TESS transits, three Spitzer transits, and 13 ground-based photometric transits of AU Mic b and three TESS transits of AU Mic c are included in the model. The following detrending parameters are treated as additive: flare (Spitzer), sky (Spitzer and PEST), and Sky/Pixel_T1 (LCO SAAO); the remaining detrending parameters are treated as multiplicative.

The Gaussian priors from Table 6 were taken from Tables 1 and 2, while the logarithmic functions were calculated; the logarithmic versions of stellar mass and orbital period were used because they are the fitted priors in EXOFASTv2. The TTV and depth offset priors were implemented to place constraints on the variation of the transit timing and depth of all light curves; any transit depth variability is not investigated further herein. Since both Pan-STARRS Y and Pan-STARRS $z_{\rm s}$ are not available among the filters in EXOFASTv2, y and z' (Sloan z) were used as respective approximate substitutes.

Given that AU Mic is a low-mass red dwarf, we configured EXOFASTv2 to use MIST for evolutionary models (Choi et al. 2016; Dotter 2016) and ignore the Claret & Bloemen limb-darkening tables (Claret & Bloemen 2011). Additionally, we incorporate the spectral energy distribution (SED) to place constraints on MIST evolutionary models; the bands and their corresponding magnitude priors are presented in Table 7. We also assume the orbit of both AU Mic b and c to be noncircular.

Table 7
Apparent Magnitude Priors for EXOFASTv2's SED Fitting of AU Mic

Band	Apparent Magnitude	References
Gaia	7.84 ± 0.02	1
$\rm Gaia_{BP}$	8.94 ± 0.02	1
$\rm Gaia_{RP}$	6.81 ± 0.02	1
$J_{\rm 2M}$	5.44 ± 0.02	2
$H_{\rm 2M}$	4.83 ± 0.02	2
$K_{\rm 2M}$	4.53 ± 0.02	3
B	10.06 ± 0.02	...
V	8.89 ± 0.18	...
$g_{\rm SDSS}$	9.58 ± 0.05	4
$r_{\rm SDSS}$	8.64 ± 0.09	4
$i_{\rm SDSS}$	7.36 ± 0.14	4

Note. This is intended to place constraints on AU Mic's MIST evolutionary models (Choi et al. 2016; Dotter 2016) and is applied only to the first of the two EXOFASTv2 runs.

References. (1) Gaia Collaboration (2018); (2) Cutri et al. (2003); (3) Stauffer et al. (2010); (4) Zacharias et al. (2012).

For the EXOFASTv2 modeling, each of the 16 observations are detrended as indicated in Table 8; Section 2 describes additional details of the detrending parameters used for each data set. We split up the EXOFASTv2 modeling into two sequential MCMC runs. For the first run, we integrate up to 15,000 steps while setting NTHIN = 12; the first run was also configured to integrate the priors from Tables 6 and 7 and invoke the rejectflatmodel option for all light curves with NTEMPS = 8 to aid in faster convergence. After the first run, EXOFASTv2 generates the new prior.2 file, which we then implement while repeating the process to achieve better convergence. For the second run, we integrate up to 20,000 steps while setting NTHIN = 5, the rejectflatmodel option was turned off, and the MIST SED file was omitted. After these runs were completed, EXOFASTv2 generated the posteriors, including the transit models (Figure 2 and Tables 9–12) and midpoint times (see Table 13). Of particular note are our eccentricity posteriors of $0.079^{+0.160}_{-0.058}$ for AU Mic b and $0.114^{+0.120}_{-0.074}$ for AU Mic c, which exclude moderate-to-high eccentricities. Additional analyses of the transits individually indicates that this posterior is most constrained by the Spitzer transits presented herein.

4. TTV Analysis

In this section, we present our $O-C$ diagram and TTV dynamical modeling with Exo-Striker, considering both a two-planet model and an example three-planet model to account for the observed TTVs.

4.1. O− C Diagram

We calculate the expected midpoint times using AU Mic b's period and $T_{\rm C}$ from Gilbert et al. (2022); the period and $T_{\rm C}$ from Martioli et al. (2021) yield similar results. Using the measured and expected midpoint times, we construct the $O-C$ diagram in Figure 3. We make use of the combined transit midpoint times (Table 13), now extracted from all light curves and R-M observations through the processes described in Section 2 for data from Gilbert et al. (2022) and the R-M observations and from our own analysis in Section 3. With a $\chi^2 \gg 1$, it is readily apparent by eye that the precise Spitzer

Table 8
Detrending Parameters Incorporated into EXOFASTv2 Modeling of AU Mic b Transits

Telescope	Date (UT)	Filter	Detrending Parameter(s)	Note
Spitzer	2019-2-10	4.5 μm	x, y, noise/pixel, FWHM_x, FWHM_y, sky, linear, quadratic	1
Spitzer	2019-2-27	4.5 μm	x, y, noise/pixel, FWHM_x, FWHM_y, sky, linear, quadratic, flare	1
Spitzer	2019-9-9	4.5 μm	x, y, noise/pixel, FWHM_x, FWHM_y, sky, linear, quadratic, Gaussian	1
LCO SSO	2020-4-25	z'	Width_T1	2
LCO SSO	2020-4-25	y	AIRMASS	2
LCO SAAO	2020-5-20	z'	AIRMASS	2
LCO SAAO	2020-5-20	y	AIRMASS	2
LCO SAAO	2020-6-6	z'	AIRMASS	2
LCO SAAO	2020-6-23	z'	AIRMASS	2
PEST	2020-7-10	V	comp_flux, x_coord, y_coord, dist_center, fwhm, airmass, sky	3
Brierfield	2020-8-13	I	Meridian_Flip, X(FITS)_T1, Y(FITS)_T1, tot_C_cnts	2
LCO SSO	2020-8-13	z'	AIRMASS, Width_T1	2
LCO SAAO	2020-9-7	z'	Width_T1, Sky/Pixel_T1	2
LCO SSO	2020-9-16	z'	Width_T1	2
LCO SSO	2020-10-3	z'	Width_T1	2
LCO SAAO	2020-10-11	z'	Width_T1	2

Notes. The flare (Spitzer), sky (Spitzer and PEST), and Sky/Pixel_T1 (LCO SAAO) were implemented as additives; the remaining detrending parameters were implemented as multiplicative. See Section 2 for details on the detrending parameters used for each observation. Since both Pan-STARRS Y and Pan-STARRS z_s are not available among the filters in EXOFASTv2, y and z' (Sloan z) were used as respective approximate substitutes.
[a] See Section 2.2 for details on the detrending parameters applied to Spitzer data.
[b] Detrending parameters generated from AIJ (Collins et al. 2017).
[c] Detrending parameters generated from PEST pipeline (http://pestobservatory.com/the-pest-pipeline).

transit times are significantly deviant from those expected from a linear ephemeris from the TESS transit times alone. Note that the Spitzer transit times are in BJD and corrected for the relative light-time travel delay between Spitzer and the solar system barycenter. Additionally, the ground-based R-M transit midpoints are similarly late and consistent with the Spitzer transit times. The ground-based photometric transits show large scatter and correspondingly larger timing uncertainties relative to the space-based transit midpoint times.

4.2. TTV Exo-Striker Dynamical Modeling

Motivated by the apparent TTV variability deviating from a linear ephemeris in Section 4.1, we utilize the Exo-Striker package (Trifonov 2019) to model the variation in transit timings of AU Mic b and c. Like EXOFASTv2, Exo-Striker utilizes an MCMC to assess the statistical significance of the measured TTVs and the confidence in the dynamical model posteriors that can be inferred from the TTVs. Additionally, we incorporate the stellar priors from Table 14 and the planet priors from Table 15.

We configured Exo-Striker to use the Simplex and Dynamical algorithms during both the model fitting and MCMC runs; the justification for using Dynamical instead of Keplerian is that the Keplerian algorithm does not work as well in a compact system with orbital resonances (Fabrycky 2010) like AU Mic. The dynamical model time steps have been set to the lowest possible 0.01 day given the short orbital periods of both planets. To find the best-fit TTV model, we employ Exo-Striker's built-in scipy minimizer algorithms. We use a truncated Newton algorithm[59] as a primary minimizer and a Nelder–Mead algorithm[60] as a secondary minimizer, with both set at one consecutive integration and 5000 integration steps; the rest of the configurations for those minimizers are left to default settings. After we find a best-fit model, we compute an MCMC with 50,000 burn-ins, 200,000 integration steps, and four walkers; the other settings for MCMC are left to defaults, including adopting 68.300% confidence intervals for estimating 1σ posterior uncertainties. These best-fit and MCMC configurations apply to both the two- and three-planet dynamical models presented herein.

We first explore the two-planet scenario (AUMic b and c). Then, we explore a representative three-planet scenario. The following subsections detail the process of exploring these cases.

4.2.1. Two-planet Dynamical Modeling

We explored a best-fit scenario for a two-planet model with Exo-Striker. The eccentricity posteriors from the EXOFASTv2 analysis (Table 9) provided us $\sim 4.056\sigma$ upper limits on both planets' eccentricity. Analysis of the transit light curves themselves excludes such high eccentricities as in Plavchan et al. (2020) and Gilbert et al. (2022), but we are only modeling the transit midpoint times herein. We also explored a best-fit scenario for a "massless" no-TTV two-planet model with Exo-Striker as a control on testing for the presence and statistical significance of TTVs.

4.2.2. Three-planet Dynamical Modeling

Cale et al. (2021) explored the analysis of the RVs of AU Mic and searched for additional candidate nontransiting planet signals. In particular, Cale et al. (2021) identified a candidate RV signal in between the orbits of AU Mic b and c with an orbital period of 12.742 days, which to date is unconfirmed, that we call a hypothetical "d" planet. This "middle-d" nontransiting planet scenario, if confirmed, would establish the AU Mic planetary system in a 4:6:9 orbital resonant chain.

[59] https://docs.scipy.org/doc/scipy/reference/optimize.minimize-tnc.html
[60] https://docs.scipy.org/doc/scipy/reference/optimize.minimize-neldermead.html

Table 9
EXOFASTv2-generated Median Values and 68% Confidence Interval for AU Mic System

Posterior	Description	Unit	Quantity	
			AU Mic b	AU Mic c
$M_\star$	Stellar mass	$M_\odot$	$0.558^{+0.068}_{0.090}$	
$R_\star$	Stellar radius	$R_\odot$	$0.749^{+0.030}_{-0.037}$	
$L_\star$	Stellar luminosity	$L_\odot$	$0.094^{+0.014}_{-0.015}$	
$\rho_\star$	Stellar density	g cm^{-3}	$1.89^{+0.24}_{-0.21}$	
$\log g$	Surface gravity	⋯	$4.443^{+0.044}_{-0.048}$	
$T_{\rm eff}$	Effective temperature	K	3701^{+100}_{-98}	
[Fe/H]	Metallicity	⋯	$0.17^{+0.27}_{-0.37}$	
$[{\rm Fe/H}]_0$	Initial metallicity[a]	⋯	$0.12^{+0.24}_{-0.36}$	
Age	⋯	Gyr	$0.0216^{+0.0034}_{-0.0031}$	
EEP	Equal evolutionary phase[b]	⋯	$164.9^{+5.4}_{-5.8}$	
$P_{\rm orb}$	Orbital period	days	$8.462993^{+0.000048}_{-0.000039}$	$18.859005^{+0.000084}_{-0.000072}$
$M_{\rm p}$	Planetary mass[c]	$M_{\rm J}$	$0.058^{+0.021}_{-0.016}$	$0.0291^{+0.0110}_{0.0080}$
$R_{\rm p}$	Planetary radius	$R_{\rm J}$	$0.373^{+0.017}_{-0.021}$	$0.250^{+0.013}_{-0.015}$
$T_{\rm C}$	Time of conjunction[d]	BJD_TDB	$2{,}458{,}330.3916^{+0.0031}_{-0.0030}$	$2{,}458{,}342.2238^{+0.0026}_{-0.0023}$
$T_{\rm T}$	Time of minimum projected separation[e]	BJD_TDB	$2{,}458{,}330.3916^{+0.0031}_{-0.0030}$	$2{,}458{,}342.2238^{+0.0026}_{-0.0023}$
T_0	Optimal conjunction time[f]	BJD_TDB	$2{,}458{,}457.3365^{+0.0031}_{-0.0029}$	$2{,}458{,}455.3777^{+0.0027}_{-0.0022}$
a	Semimajor axis	au	$0.0669^{+0.0026}_{-0.0038}$	$0.1141^{+0.0044}_{-0.0065}$
e	Eccentricity	⋯	$0.079^{+0.160}_{-0.058}$	$0.114^{+0.120}_{-0.074}$
i	Inclination	deg	$89.72^{+0.22}_{-0.29}$	$89.39^{+0.47}_{-0.28}$
ω	Argument of periastron	deg	-90 ± 100	-90 ± 100
$T_{\rm eq}$	Equilibrium temperature[g]	K	595^{+18}_{-21}	456^{+14}_{-16}
$\tau_{\rm circ}$	Tidal circularization timescale	Gyr	152^{+81}_{-55}	16400^{+9000}_{-7500}
K	RV semiamplitude[c]	m s^{-1}	$8.6^{+3.2}_{-2.4}$	$3.33^{+1.30}_{-0.92}$
$R_{\rm p}/R_\star$	⋯	⋯	$0.05137^{+0.00099}_{-0.00120}$	$0.03429^{+0.00100}_{-0.00099}$
$a/R_\star$	⋯	⋯	$19.28^{+0.79}_{-0.73}$	32.9 ± 1.3
δ	Transit depth $(R_{\rm p}/R_\star)^2$	⋯	$0.00264^{+0.00010}_{-0.00012}$	$0.001176^{+0.000070}_{-0.000067}$
$\delta_{\rm I}$	Transit depth in I	⋯	$0.00366^{+0.00130}_{-0.00072}$	$0.00152^{+0.00048}_{-0.00027}$
$\delta_{z'}$	Transit depth in z'	⋯	$0.00409^{+0.00053}_{-0.00044}$	$0.00169^{+0.00020}_{-0.00018}$
$\delta_{4.5\mu{\rm m}}$	Transit depth in 4.5 μm	⋯	$0.00265^{+0.00010}_{-0.00012}$	$0.001182^{+0.000069}_{-0.000068}$
$\delta_{\rm TESS}$	Transit depth in TESS	⋯	$0.00339^{+0.00019}_{-0.00022}$	$0.001462^{+0.000077}_{-0.000093}$
δ_V	Transit depth in V	⋯	$0.00341^{+0.0014}_{-0.00058}$	$0.00146^{+0.00051}_{-0.00024}$
δ_y	Transit depth in y	⋯	$0.00357^{+0.00160}_{-0.00068}$	$0.00149^{+0.00057}_{-0.00025}$
τ	Ingress/egress transit duration	days	$0.00721^{+0.00022}_{-0.00025}$	$0.00664^{+0.00180}_{-0.00084}$
T_{14}	Total transit duration	days	$0.14585^{+0.00031}_{-0.00036}$	$0.1773^{+0.0017}_{-0.0015}$
$T_{\rm FWHM}$	FWHM transit duration	days	$0.13861^{+0.00020}_{-0.00023}$	$0.1703^{+0.0011}_{-0.0013}$
b	Transit impact parameter	⋯	$0.098^{+0.092}_{-0.065}$	$0.35^{+0.19}_{-0.26}$
$b_{\rm S}$	Eclipse impact parameter	⋯	$0.093^{+0.091}_{-0.063}$	$0.346^{+0.095}_{-0.260}$
$\tau_{\rm S}$	Ingress/egress eclipse duration	days	$0.00715^{+0.00059}_{-0.00070}$	$0.00647^{+0.00061}_{-0.00065}$
$T_{\rm S,14}$	Total eclipse duration	days	$0.145^{+0.011}_{-0.014}$	$0.173^{+0.020}_{-0.027}$
$T_{\rm S,FWHM}$	FWHM eclipse duration	days	$0.137^{+0.010}_{-0.014}$	$0.166^{+0.020}_{-0.026}$
$\delta_{\rm S,2.5\mu m}$	Blackbody eclipse depth at 2.5 μm	ppm	$0.63^{+0.18}_{-0.16}$	$0.0147^{+0.0060}_{-0.0051}$
$\delta_{\rm S,5.0\mu m}$	Blackbody eclipse depth at 5.0 μm	ppm	$24.9^{+3.3}_{-3.4}$	$2.55^{+0.48}_{-0.49}$
$\delta_{\rm S,7.5\mu m}$	Blackbody eclipse depth at 7.5 μm	ppm	$74.3^{+6.7}_{-7.4}$	$12.2^{+1.5}_{-1.7}$
$\rho_{\rm p}$	Planetary density[c]	g cm^{-3}	$1.42^{+0.60}_{-0.35}$	$2.28^{+0.94}_{-0.62}$
$\log g_{\rm p}$	Surface gravity[c]	⋯	$3.02^{+0.14}_{-0.12}$	$3.07^{+0.14}_{-0.11}$
Θ	Safronov number	⋯	$0.0373^{+0.0140}_{-0.0097}$	$0.048^{+0.019}_{-0.013}$
$\langle F \rangle$	Incident flux	10^9 $\frac{\rm erg}{\rm s\ cm^2}$	$0.0282^{+0.0035}_{-0.0039}$	0.0096 ± 0.0013
$T_{\rm P}$	Time of periastron	BJD_TDB	$2458323.3^{+2.7}_{-3.0}$	$2458332.8^{+6.1}_{-6.2}$
$T_{\rm S}$	Time of eclipse	BJD_TDB	$2458334.62^{+0.54}_{-0.50}$	$2{,}458{,}332.8 \pm 1.3$
$T_{\rm A}$	Time of ascending node	BJD_TDB	$2458328.27^{+0.30}_{-0.48}$	$2458337.41^{+0.72}_{-1.20}$
$T_{\rm D}$	Time of descending node	BJD_TDB	$2458332.51^{+0.50}_{-0.28}$	$2458347.03^{+1.20}_{-0.72}$
$V_{\rm c}/V_{\rm e}$	h	⋯	$1.000^{+0.045}_{-0.038}$	$1.009^{+0.140}_{-0.060}$
$\sqrt{\left(1-\frac{R_{\rm p}}{R_\star}\right)^2-{\rm b}^2}$	Transit chord	⋯	$1.0466^{+0.0042}_{-0.0130}$	$0.974^{+0.050}_{-0.092}$
Sign	i	⋯	$1.40^{+0.40}_{-0.33}$	$1.48^{+0.33}_{-0.34}$
$e\cos\omega$	⋯	⋯	$-0.001^{+0.100}_{-0.093}$	$0.00^{+0.10}_{-0.11}$

Table 9
(Continued)

Posterior	Description	Unit	Quantity	
			AU Mic b	AU Mic c
$e \sin\omega$	...	...	$-0.004^{+0.037}_{-0.054}$	$-0.015^{+0.060}_{-0.14}$
$M_p \sin i$	Minimum mass[c]	M_J	$0.058^{+0.021}_{-0.016}$	$0.0291^{+0.0110}_{-0.0080}$
$M_p/M_\star$	Mass ratio[c]	...	$0.000099^{+0.000039}_{-0.000028}$	$0.000050^{+0.000021}_{-0.000014}$
$d/R_\star$	Separation at mid-transit	...	$19.2^{+1.6}_{-1.5}$	$33.1^{+4.2}_{-2.7}$
P_T	A priori nongrazing transit probability	...	$0.0495^{+0.0043}_{-0.0038}$	$0.0291^{+0.0026}_{-0.0033}$
$P_{T,G}$	A priori transit probability	...	$0.0548^{+0.0047}_{-0.0041}$	$0.0312^{+0.0028}_{-0.0035}$
P_S	A priori nongrazing eclipse probability	...	$0.04958^{+0.00210}_{-0.00067}$	$0.0299^{+0.0038}_{-0.0020}$
$P_{S,G}$	A priori eclipse probability	...	$0.05492^{+0.00240}_{-0.00073}$	$0.0320^{+0.0042}_{-0.0021}$
$u_{1,I}$	Linear limb-darkening coefficient in I	...	$0.57^{+0.39}_{-0.36}$	
$u_{1,z'}$	Linear limb-darkening coefficient in z'	...	$0.72^{+0.13}_{-0.14}$	
$u_{1,4.5\mu m}$	Linear limb-darkening coefficient in 4.5 μm	...	$0.0086^{+0.0130}_{-0.0065}$	
$u_{1,TESS}$	Linear limb-darkening coefficient in TESS	...	$0.453^{+0.059}_{-0.064}$	
$u_{1,V}$	Linear limb-darkening coefficient in V	...	$0.47^{+0.45}_{-0.33}$	
$u_{1,y}$	Linear limb-darkening coefficient in y	...	$0.54^{+0.45}_{-0.36}$	
$u_{2,I}$	Quadratic limb-darkening coefficient in I	...	$0.01^{+0.42}_{-0.33}$	
$u_{2,z'}$	Quadratic limb-darkening coefficient in z'	...	$-0.28^{+0.17}_{-0.10}$	
$u_{2,4.5\mu m}$	Quadratic limb-darkening coefficient in 4.5 μm	...	$0.140^{+0.037}_{-0.038}$	
$u_{2,TESS}$	Quadratic limb-darkening coefficient in TESS	...	$0.207^{+0.100}_{-0.097}$	
$u_{2,V}$	Quadratic limb-darkening coefficient in V	...	$0.09^{+0.45}_{-0.37}$	
$u_{2,y}$	Quadratic limb-darkening coefficient in y	...	$0.02^{+0.40}_{-0.34}$	

Notes. See Table 3 in Eastman et al. (2019) for a detailed description of all parameters. Since both Pan-STARRS Y and Pan-STARRS z_s are not available among the filters in EXOFASTv2, y and z' (Sloan z) were used as respective approximate substitutes. Additionally, the Claret & Bloemen limb-darkening tables (Claret & Bloemen 2011) default option has been disabled, since AU Mic is a low-mass red dwarf.
[a] The metallicity of the star at birth.
[b] Corresponds to static points in a star's evolutionary history. See Section 2 in Dotter (2016).
[c] Uses measured radius and estimated mass from Chen & Kipping (2017).
[d] Time of conjunction is commonly reported as the "transit time."
[e] Time of minimum projected separation is a more correct transit time.
[f] Optimal time of conjunction minimizes the covariance between T_C and period.
[g] Assumes no albedo and perfect redistribution.
[h] The velocity at T_C of an assumed circular orbit divided by the velocity of the modeled eccentric orbit.
[i] The sign of the solution to the quadratic mapping from V_c/V_e to e.

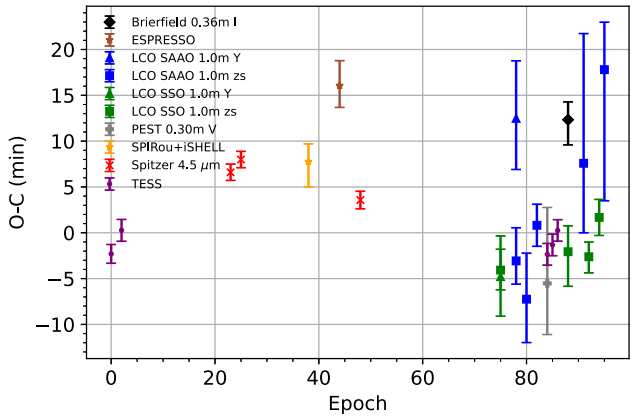

Figure 3. The $O-C$ diagram of AU Mic b using the EXOFASTv2-generated measured midpoint times and the calculated expected midpoint times for all 23 AU Mic b transit data sets from Table 3. For the calculation of expected midpoint times, AU Mic b's period and T_C from Gilbert et al. (2022) were used.

This would not be the first known nontransiting planet to exist between two transiting planets; Christiansen et al. (2017), Buchhave et al. (2016), Sun et al. (2019), and Osborn et al. (2021) identified similar exoplanet configurations for the HD 3167, Kepler-20, Kepler-411, and TOI-431 planetary systems, respectively. Similarly to the two-planet model, we imposed 4σ upper limits on the eccentricity of planets b and c for this paper.

4.3. TTV Results

Here we present the results of both the no-TTV two-planet and three-planet TTV modeling using the Exo-Striker package. We also calculate the mass of AU Mic c using the generated posteriors from Exo-Striker.

4.3.1. Results of Exo-Striker Two-planet Modeling

The best-fit $O-C$ diagram (Figure 4), posteriors (Table 16), and MCMC corner plot (Figure A1) showcase the best possible two-planet model. The Exo-Striker angular momentum deficit (AMD; Laskar 1997, 2000; Laskar & Petit 2017) criterion indicated that the two-planet model is stable. However, it is clear from Figure 4 that the model does not converge very well with the data points, especially with TESS and Spitzer. This implies that we potentially need a third planet to account for the observed TTV variability. This interpretation is one of several hypotheses that are being explored and are

Table 10
EXOFASTv2-generated Median Values and 68% Confidence Interval for Follow-up Observations of AU Mic Transits (Part I)

Planet	Telescope	Date (UT)	Filter	σ^2 (Added Variance)	TTV (days)	$T\delta V$[a]	F_0[b]
b	TESS	2018-7-26	TESS	$0.0000000019^{+0.0000000100}_{-0.0000000088}$	$-0.0024^{+0.0028}_{-0.0031}$	$-0.0006^{+0.0013}_{-0.0012}$	$1.000002^{+0.000024}_{-0.000023}$
c	TESS	2018-8-11	TESS	$0.0000000030 \pm 0.0000000097$	$-0.0005^{+0.0020}_{-0.0026}$	$-0.00006^{+0.00080}_{-0.00074}$	$0.999994^{+0.000026}_{-0.000027}$
b	TESS	2018-8-12	TESS	$0.000000005^{+0.000000016}_{-0.000000013}$	$-0.0006^{+0.0029}_{-0.0030}$	$-0.0006^{+0.0014}_{-0.0012}$	0.999999 ± 0.000030
b	Spitzer	2019-2-10	4.5 μm	$0.0000000600^{+0.0000000050}_{-0.0000000047}$	0.0039 ± 0.0030	$-0.00853^{+0.00130}_{-0.00100}$	1.000075 ± 0.000022
b	Spitzer	2019-2-27	4.5 μm	$0.0000000374^{+0.0000000040}_{-0.0000000036}$	$0.0049^{+0.0029}_{-0.0031}$	$-0.0055^{+0.0015}_{-0.0012}$	$1.000220^{+0.000019}_{-0.000017}$
b	Spitzer	2019-9-9	4.5 μm	$0.0000000933^{+0.0000000042}_{-0.0000000037}$	$0.0020^{+0.0032}_{-0.0035}$	$-0.0039^{+0.0014}_{-0.0011}$	$0.999893^{+0.000013}_{-0.000014}$
b	LCO SSO	2020-4-25	z'	$0.00000234^{+0.00000029}_{-0.00000028}$	$-0.0028^{+0.0040}_{-0.0048}$	$-0.0054^{+0.0047}_{-0.0032}$	$1.00000^{+0.00013}_{-0.00014}$
b	LCO SSO	2020-4-25	y	$0.00000104^{+0.00000100}_{-0.00000067}$	$-0.0037^{+0.0048}_{-0.0059}$	$0.0037^{+0.0046}_{-0.0076}$	$0.99964^{+0.00031}_{-0.00038}$
b	LCO SAAO	2020-5-20	z'	$0.00000188 \pm 0.00000018$	$-0.0019^{+0.0044}_{-0.0049}$	$0.0005^{+0.0025}_{-0.0027}$	1.00034 ± 0.00018
b	LCO SAAO	2020-5-20	y	$0.00000140^{+0.00000060}_{-0.00000047}$	$0.0084^{+0.0057}_{-0.0066}$	$0.0000^{+0.0047}_{-0.0052}$	$0.99993^{+0.00044}_{-0.00039}$
b	LCO SAAO	2020-6-6	z'	$0.00000677^{+0.00000081}_{-0.00000066}$	$-0.0053^{+0.0050}_{-0.0056}$	$-0.0018^{+0.0053}_{-0.0050}$	$1.00005^{+0.00041}_{-0.00034}$
b	LCO SAAO	2020-6-23	z'	$0.00000185^{+0.00000025}_{-0.00000021}$	$0.0003^{+0.0040}_{-0.0049}$	$0.0079^{+0.0016}_{-0.0031}$	$0.99987^{+0.00018}_{-0.00021}$
c	TESS	2020-7-9	TESS	$0.000000001 \pm 0.000000015$	$-0.0024^{+0.0031}_{-0.0047}$	$0.00023^{+0.00100}_{-0.00063}$	$1.000001^{+0.000020}_{-0.000021}$
b	TESS	2020-7-10	TESS	$0.000000002^{+0.000000012}_{-0.000000011}$	$-0.0018^{+0.0038}_{-0.0047}$	$-0.0006^{+0.0013}_{-0.0011}$	$0.999999^{+0.000015}_{-0.000018}$
b	PEST	2020-7-10	V	$0.00000600^{+0.00000074}_{-0.00000076}$	-0.0038 ± 0.0061	$-0.0081^{+0.0029}_{-0.0014}$	$0.99817^{+0.00018}_{-0.00015}$
b	TESS	2020-7-19	TESS	$0.0000000015^{+0.0000000100}_{-0.0000000099}$	$-0.0009^{+0.0036}_{-0.0050}$	$-0.0006^{+0.0013}_{-0.0011}$	1.000000 ± 0.000015
b	TESS	2020-7-27	TESS	$0.0000000011 \pm 0.0000000097$	$0.0002^{+0.0037}_{-0.0050}$	$-0.0007^{+0.0013}_{-0.0011}$	0.999999 ± 0.000015
c	TESS	2020-7-28	TESS	$0.000000001^{+0.000000013}_{-0.000000012}$	$0.0001^{+0.0032}_{-0.0039}$	$0.00022^{+0.00097}_{-0.00058}$	$1.000001^{+0.000017}_{-0.000019}$
b	Brierfield	2020-8-13	I	$0.0000117^{+0.0000011}_{-0.0000010}$	$0.0085^{+0.0047}_{-0.0055}$	$0.0070^{+0.0022}_{-0.0036}$	$0.99935^{+0.00025}_{-0.00028}$
b	LCO SSO	2020-8-13	z'	$0.00000406^{+0.00000039}_{-0.00000037}$	$-0.0018^{+0.0044}_{-0.0062}$	$-0.0013^{+0.0034}_{-0.0036}$	$1.00009^{+0.00030}_{-0.00026}$
b	LCO SAAO	2020-9-7	z'	$0.00000688^{+0.00000083}_{-0.00000070}$	$0.0064^{+0.0092}_{-0.0068}$	$-0.0057^{+0.0042}_{-0.0030}$	$0.99988^{+0.00045}_{-0.00035}$
b	LCO SSO	2020-9-16	z'	$0.00000131^{+0.00000013}_{-0.00000011}$	$-0.0020^{+0.0041}_{-0.0054}$	$0.0000^{+0.0021}_{-0.0023}$	0.99996 ± 0.00013
b	LCO SSO	2020-10-3	z'	$0.00000125^{+0.00000017}_{-0.00000014}$	$0.0011^{+0.0041}_{-0.0056}$	$0.0020^{+0.0022}_{-0.0024}$	$1.00216^{+0.00017}_{-0.00016}$
b	LCO SAAO	2020-10-11	z'	$0.00000651^{+0.00000069}_{-0.00000058}$	$0.0100^{+0.0070}_{-0.0074}$	$0.0039^{+0.0030}_{-0.0033}$	$1.00099^{+0.00048}_{-0.00049}$

Notes. See Table 3 in Eastman et al. (2019) for a detailed description of all parameters. Since both Pan-STARRS Y and Pan-STARRS z_s are not available among the filters in EXOFASTv2, y and z' (Sloan z) were used as respective approximate substitutes.
[a] Transit depth variation.
[b] Baseline flux.

Table 11
EXOFASTv2-generated Median Values and 68% Confidence Interval for Follow-up Observations of AU Mic b (Part II)

Planet	Telescope	Date (UT)	Filter	C_0[a]	C_1[a]	M_0[b]	M_1[b]	M_2[b]
b	TESS	2018-7-26	TESS	⋯	⋯	⋯	⋯	⋯
c	TESS	2018-8-11	TESS	⋯	⋯	⋯	⋯	⋯
b	TESS	2018-8-12	TESS	⋯	⋯	⋯	⋯	⋯
b	Spitzer	2019-2-10	4.5 μm	$-0.000165^{+0.000043}_{-0.000041}$	⋯	$-0.00110^{+0.00034}_{-0.00033}$	-0.0112 ± 0.0010	0.0108 ± 0.0010
b	Spitzer	2019-2-27	4.5 μm	$-0.000247^{+0.000044}_{-0.000042}$	$0.000048^{+0.000041}_{-0.000032}$	$0.00070^{+0.00033}_{-0.00037}$	$0.00037^{+0.00037}_{-0.00041}$	$-0.00303^{+0.00081}_{-0.00076}$
b	Spitzer	2019-9-9	4.5 μm	$-0.000576^{+0.000093}_{-0.000110}$	⋯	-0.00030 ± 0.00016	$0.00194^{+0.00020}_{-0.00021}$	$-0.00022^{+0.00061}_{-0.00063}$
b	LCO SSO	2020-4-25	z'	⋯	⋯	$0.00000^{+0.00024}_{-0.00026}$	⋯	⋯
b	LCO SSO	2020-4-25	y	⋯	⋯	$-0.00111^{+0.00074}_{-0.00079}$	⋯	⋯
b	LCO SAAO	2020-5-20	z'	⋯	⋯	0.00102 ± 0.00035	⋯	⋯
b	LCO SAAO	2020-5-20	y	⋯	⋯	$-0.00007^{+0.00071}_{-0.00070}$	⋯	⋯
b	LCO SAAO	2020-6-6	z'	⋯	⋯	$0.00025^{+0.00081}_{-0.00074}$	⋯	⋯
b	LCO SAAO	2020-6-23	z'	⋯	⋯	$-0.00021^{+0.00038}_{-0.00049}$	⋯	⋯
c	TESS	2020-7-9	TESS	⋯	⋯	⋯	⋯	⋯
b	TESS	2020-7-10	TESS	⋯	⋯	⋯	⋯	⋯
b	PEST	2020-7-10	V	$-0.0037^{+0.0050}_{-0.0049}$	⋯	0.1038 ± 0.0040	-0.1074 ± 0.0043	$-0.0002^{+0.0017}_{-0.0016}$
b	TESS	2020-7-19	TESS	⋯	⋯	⋯	⋯	⋯
b	TESS	2020-7-27	TESS	⋯	⋯	⋯	⋯	⋯
c	TESS	2020-7-28	TESS	⋯	⋯	⋯	⋯	⋯
b	Brierfield	2020-8-13	I	⋯	⋯	-0.0038 ± 0.0052	$-0.0026^{+0.0045}_{-0.0047}$	$-0.0009^{+0.0022}_{-0.0023}$
b	LCO SSO	2020-8-13	z'	⋯	⋯	$-0.00002^{+0.00043}_{-0.00052}$	$0.00028^{+0.00029}_{-0.00033}$	⋯
b	LCO SAAO	2020-9-7	z'	$-0.00020^{+0.00063}_{-0.00066}$	⋯	-0.00035 ± 0.00096	⋯	⋯
b	LCO SSO	2020-9-16	z'	⋯	⋯	$0.00014^{+0.00033}_{-0.00029}$	⋯	⋯
b	LCO SSO	2020-10-03	z'	⋯	⋯	-0.00179 ± 0.00028	⋯	⋯
b	LCO SAAO	2020-10-11	z'	⋯	⋯	-0.0014 ± 0.0016	⋯	⋯

Notes. See Table 3 in Eastman et al. (2019) for a detailed description of all parameters. Since both Pan-STARRS Y and Pan-STARRS z_s are not available among the filters in EXOFASTv2, y and z' (Sloan z) were used as respective approximate substitutes. Also see Section 2 of this paper for details on the detrending parameters used for each observation; the flare (Spitzer), sky (Spitzer and PEST), and Sky/Pixel_T1 (LCO SAAO) were set as additive, while the remaining detrending parameters were set as multiplicative.
[a] Additive detrending coefficient.
[b] Multiplicative detrending coefficient.

Table 12
EXOFASTv2-generated Median Values and 68% Confidence Interval for Follow-up Observations of AU Mic b (Part III)

Planet	Telescope	Date (UT)	Filter	M_3[a]	M_4[a]	M_5[a]	M_6[a]	M_7[a]
b	TESS	2018-7-26	TESS	⋯	⋯	⋯	⋯	⋯
c	TESS	2018-8-11	TESS	⋯	⋯	⋯	⋯	⋯
b	TESS	2018-8-12	TESS	⋯	⋯	⋯	⋯	⋯
b	Spitzer	2019-2-10	4.5 μm	$-0.00623^{+0.00075}_{-0.00074}$	0.00496 ± 0.00048	$-0.000407^{+0.000041}_{-0.000042}$	$-0.000270^{+0.000057}_{-0.000053}$	⋯
b	Spitzer	2019-2-27	4.5 μm	$0.00326^{+0.00073}_{-0.00080}$	$0.00118^{+0.00065}_{-0.00060}$	$0.000873^{+0.000095}_{-0.000110}$	$-0.00088^{+0.00015}_{-0.00013}$	⋯
b	Spitzer	2019-9-9	4.5 μm	0.00049 ± 0.00056	$-0.00174^{+0.00046}_{-0.00045}$	$-0.000003^{+0.000044}_{-0.000046}$	$-0.000403^{+0.000061}_{-0.000057}$	$-0.000519^{+0.000059}_{-0.000058}$
b	LCO SSO	2020-4-25	z'	⋯	⋯	⋯	⋯	⋯
b	LCO SSO	2020-4-25	y	⋯	⋯	⋯	⋯	⋯
b	LCO SAAO	2020-5-20	z'	⋯	⋯	⋯	⋯	⋯
b	LCO SAAO	2020-5-20	y	⋯	⋯	⋯	⋯	⋯
b	LCO SAAO	2020-6-6	z'	⋯	⋯	⋯	⋯	⋯
b	LCO SAAO	2020-6-23	z'	⋯	⋯	⋯	⋯	⋯
c	TESS	2020-7-9	TESS	⋯	⋯	⋯	⋯	⋯
b	TESS	2020-7-10	TESS	⋯	⋯	⋯	⋯	⋯
b	PEST	2020-7-10	V	$0.0004^{+0.0012}_{-0.0014}$	$-0.0023^{+0.0028}_{-0.0026}$	0.0013 ± 0.0011	$-0.00284^{+0.00088}_{-0.00087}$	⋯
b	TESS	2020-7-19	TESS	⋯	⋯	⋯	⋯	⋯
b	TESS	2020-7-27	TESS	⋯	⋯	⋯	⋯	⋯
c	TESS	2020-7-28	TESS	⋯	⋯	⋯	⋯	⋯
b	Brierfield	2020-8-13	I	$-0.0009^{+0.0015}_{-0.0014}$	⋯	⋯	⋯	⋯
b	LCO SSO	2020-8-13	z'	⋯	⋯	⋯	⋯	⋯
b	LCO SAAO	2020-9-7	z'	⋯	⋯	⋯	⋯	⋯
b	LCO SSO	2020-9-16	z'	⋯	⋯	⋯	⋯	⋯
b	LCO SSO	2020-10-3	z'	⋯	⋯	⋯	⋯	⋯
b	LCO SAAO	2020-10-11	z'	⋯	⋯	⋯	⋯	⋯

Note. See Table 3 in Eastman et al. (2019) for a detailed description of all parameters. Since both Pan-STARRS Y and Pan-STARRS z_s are not available among the filters in EXOFASTv2, y and z' (Sloan z) were used as respective approximate substitutes. Also see Section 2 of this paper for details on the detrending parameters used for each observation; the flare (Spitzer), sky (Spitzer and PEST), and Sky/Pixel_T1 (LCO SAAO) were set as additive, while the remaining detrending parameters were set as multiplicative.
[a] Multiplicative detrending coefficient.

discussed in greater detail in Section 6. For our control no-TTV scenario of massless planets b and c, we present the best-fit $O-C$ diagram (Figure 5), posteriors (Table 17), and corner plot (Figure A2).

4.3.2. Results of Exo-Striker Three-planet Modeling

Since the two-planet circular orbit model does not adequately reproduce the observed TTVs, as evidenced in Figure 4, we explored a representative and nonexhaustive hypothetical three-planet scenario. We find a best-fit and MCMC model for this representative three-planet scenario that adequately accounts for the TESS and Spitzer TTVs and is also consistent with the RV candidate signal in Cale et al. (2021), presented in Table 18 and Figures 6 and A3. Moreover, the three-planet case's log-likelihood, χ^2, and reduced χ^2 are better than those of the two-planet case, the latter of which are better than the no-TTV massless scenario (Table 19). The delta log-likelihoods and corresponding ΔAICc indicate that the three-planet scenario is strongly favored, and the two-planet and no-TTV scenarios are statistically excluded. Exo-Striker indicates that this three-planet solution fails the AMD criterion. However, given the 4:6:9 orbital period commensurability for b, d, and c, respectively, we investigate the dynamical stability of this system configuration with two N-body codes, the latter of which is used for a consistency check. We generate simulations with rebound (Rein & Liu 2012; Rein & Spiegel 2015) and mercury6 (Chambers 1999) to test the stability of this representative three-planet system; both indicate that this three-planet configuration is stable (see Section 6 for more detailed discussions).

4.3.3. The Mass of AU Mic c

We use Equation (1) from Cumming et al. (1999) and the best-fit parameters and MCMC uncertainties from Tables 16 and 18 to calculate the mass of AU Mic c. To simplify the equation, we made an assumption that $M_\star \gg M_p$. For the best-fit two-planet scenario, our calculation yields a mass of c of $0.0781 \pm 0.0039\ M_J$ (or $24.8 \pm 1.2\ M_\oplus$) at 20.7σ significance, which makes it a roughly Neptune-sized planet. In the case of our representative three-planet scenario, our calculation yields a mass of c of $0.0631 \pm 0.0049\ M_J$ (or $20.1 \pm 1.6\ M_\oplus$) at 12.6σ significance, implying that it again has roughly the mass of Neptune.

5. Photodynamical Analysis

In a second independent analysis to validate our methods, we used a photodynamical code to simultaneously fit the transit light curves and TTVs. The core of this code is based on rebound (Rein & Liu 2012; Rein & Spiegel 2015), with which the N-body problem is integrated using the high-accuracy nonsymplectic integrator with adaptive time stepping IAS15. At the times of the measured mid-transit times, the current orbital elements are used to calculate the corresponding transit light curve using the python implementation of the model from Mandel & Agol (2002) from Ian Crossfield.[61]

[61] https://www.lpl.arizona.edu/~ianc/python/_modules/transit.html

Table 13
AU Mic Planets' Midpoint Time Priors for `Exo-Striker` Models

Planet	Telescope	Transit N	Date (UT)	Band	T_0 (BJD)
b	TESS	1	2018-7-26	TESS	2,458,330.38920 ± 0.00041
	TESS	3	2018-8-12	TESS	2,458,347.31699 ± 0.00060
	Spitzer	24	2019-2-10	4.5 μm	2,458,525.04439 ± 0.00017
	Spitzer	26	2019-2-27	4.5 μm	2,458,541.97136 ± 0.00016
	SPIRou + iSHELL	39	2019-6-17	(a)	2,458,651.99020 ± 0.00180
	ESPRESSO	45	2019-8-7	378.2–788.7 nm	2,458,702.77397 ± 0.00178
	Spitzer	49	2019-9-9	4.5 μm	2,458,736.61730 ± 0.00015
	LCO SSO	76	2020-4-25	Pan-STARRS Y	2,458,965.11250 ± 0.00300
	LCO SSO	76	2020-4-25	Pan-STARRS z_s	2,458,965.11300 ± 0.00140
	LCO SAAO	79	2020-5-20	Pan-STARRS z_s	2,458,990.50270 ± 0.00240
	LCO SAAO	79	2020-5-20	Pan-STARRS Y	2,458,990.51350 ± 0.00430
	LCO SAAO	81	2020-6-6	Pan-STARRS z_s	2,459,007.42580 ± 0.00340
	LCO SAAO	83	2020-6-23	Pan-STARRS z_s	2,459,024.35740 ± 0.00140
	PEST	85	2020-7-10	V	2,459,041.27900 ± 0.00570
	TESS	85	2020-7-10	TESS	2,459,041.28120 ± 0.00030
	TESS	86	2020-7-19	TESS	2,459,049.74491 ± 0.00028
	TESS	87	2020-7-27	TESS	2,459,058.20901 ± 0.00026
	LCO SSO	89	2020-8-13	Pan-STARRS z_s	2,459,075.13340 ± 0.00250
	Brierfield	89	2020-8-13	I	2,459,075.14340 ± 0.00240
	LCO SAAO	92	2020-9-7	Pan-STARRS z_s	2,459,100.52910 ± 0.00980
	LCO SSO	93	2020-9-16	Pan-STARRS z_s	2,459,108.98502 ± 0.00092
	LCO SSO	95	2020-10-3	Pan-STARRS z_s	2,459,125.91400 ± 0.00110
	LCO SAAO	96	2020-10-11	Pan-STARRS z_s	2,459,134.38820 ± 0.00990
c	TESS	1	2018-8-11	TESS	2,458,342.22330 ± 0.00110
	TESS	38	2020-7-9	TESS	2,459,040.00432 ± 0.00082
	TESS	39	2020-7-28	TESS	2,459,058.86603 ± 0.00072

Note. (a) 955–2515 nm (SPIRou) and 2.18–2.47 nm (iSHELL).

Table 14
AU Mic's Stellar Priors for `Exo-Striker` Best-fit and MCMC Modeling

Prior	Unit	AU Mic
Mass	$M_\odot$	$\mathcal{N}(0.50, 0.03)$
Radius	$R_\odot$	$\mathcal{N}(0.75, 0.03)$
Luminosity	$L_\odot$	$\mathcal{N}(0.0900, 0.0001)$
$T_{\rm eff}$	K	$\mathcal{N}(3700, 100)$
$v \sin i$	km s^{-1}	$\mathcal{N}(8.7, 0.2)$

Note. These priors are taken from Plavchan et al. (2020).

Table 15
AU Mic's Planetary Priors for `Exo-Striker` Best-fit and MCMC Modeling

Prior	Unit	AU Mic b	AU Mic c	AU Mic d[a]
K	m s^{-1}	$\mathcal{N}(8.5, 2.3)$	$\mathcal{U}(0.8, 9.5)$	$\mathcal{U}(0.0, 10000.0)$
$P_{\rm orb}$	day	$\mathcal{N}(8.463, 0.001)$	$\mathcal{N}(18.859, 0.001)$	$\mathcal{N}(12.742, 0.020)$
e	⋯	$\mathcal{U}(0.00000, 0.58038)$	$\mathcal{U}(0.00000, 0.37308)$	$\mathcal{U}(0.000, 0.999)$
ω	deg	$\mathcal{U}(0.0, 360.0)$	$\mathcal{U}(0.0, 360.0)$	$\mathcal{U}(0.0, 360.0)$
M_0	deg	$\mathcal{U}(0.0, 360.0)$	$\mathcal{U}(0.0, 360.0)$	$\mathcal{U}(0.0, 360.0)$
i	deg	$\mathcal{N}(89.5, 0.3)$	$\mathcal{N}(89.0, 0.5)$	$\mathcal{U}(0.0, 180.0)$
Ω	deg	$\mathcal{U}(0.0, 360.0)$	$\mathcal{U}(0.0, 360.0)$	$\mathcal{U}(0.0, 360.0)$

Note. $M_0 \equiv$ mean anomaly, and $\Omega \equiv$ longitude of ascending node.
[a] For three-planet model only.

Using the MCMC sample `emcee` (Foreman-Mackey et al. 2013), we sample the parameter space maximizing the log-likelihood. In addition to the transit light curves, the code also fits the RV data of AU Mic taken with SPIRou (Cale et al. 2021; Klein et al. 2021), which at NIR wavelengths is least impacted by the stellar activity of this young system. The RV model is calculated from the same `rebound`N-body integration of the planetary system. As free parameters, we have the planetary masses, orbital periods, eccentricities, longitudes of periastron, inclination, and $R_{\rm p}/R_\star$ ratio. The stellar mass and radius, and hence the stellar density, are fixed. The limb darkening for the various bands is taken from Claret et al. (2012) and Claret (2017) and kept at the literature values. Since the Spitzer transits show depth variations, we account for this effect by a third light contribution as free parameter (to be explored further in future work). All data sets have their individual offsets, while the SPIRou data are modeled by adding a "jitter" white-noise term.

The stellar activity is modeled using `celerite` (Foreman-Mackey et al. 2017), which has the advantage of offering a fast and scalable implementation of GP regression, especially important for large data sets. The `celerite` package provides several built-in covariance kernels; one represents damped oscillations driven by white noise called `SHO`. It has three parameters: the undamped oscillator frequency or period $\omega_0 = 2\pi/P$, the quality factor Q of the oscillator (which is reversely proportional to the damping timescale τ), and the variance S_0. For more details, see Equations (19)–(24) in Foreman-Mackey et al. (2017). Starspots typically manifest in variations at the rotation period, as well as on the first harmonic. In order to represent this in a rotational kernel, we follow the idea presented in `celerite2` (Foreman-Mackey

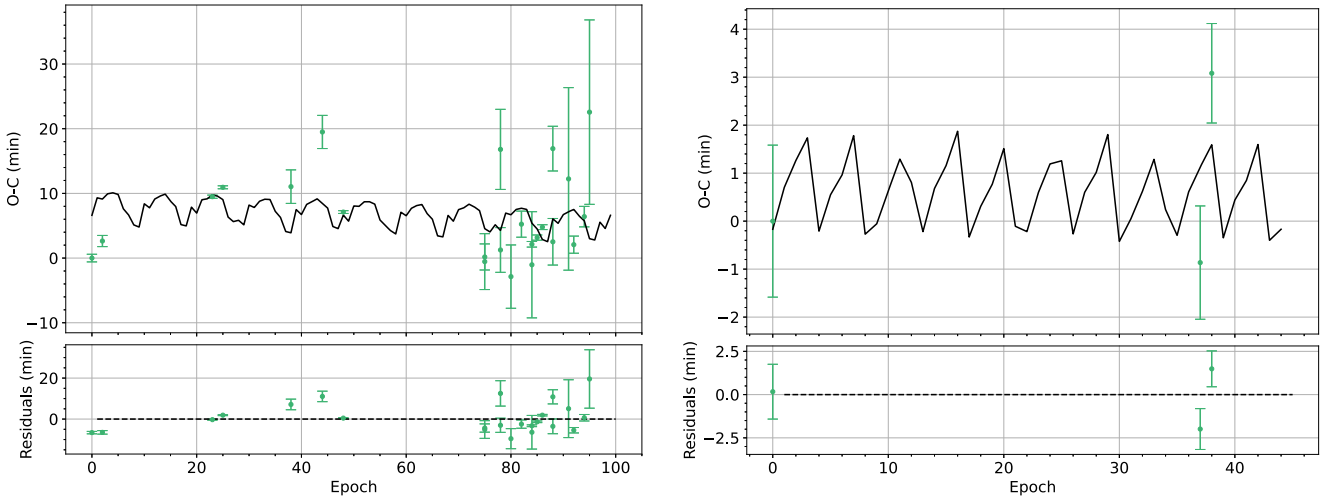

Figure 4. Two-planet $O-C$ diagram of AU Mic b (left) and AU Mic c (right), with comparison between TTVs (green) and `Exo-Striker`-generated best-fit models (black).

Table 16
`Exo-Striker`-generated Parameters for AU Mic Two-planet Best-fit and MCMC Modeling

Parameter	Unit	Best-fit		MCMC	
		AU Mic b	AU Mic c	AU Mic b	AU Mic c
K	m s^{-1}	4.03906	9.49903	4.10830 ± 1.47951	9.31429 ± 0.27661
$P_{\rm orb}$	day	8.46255	18.86109	8.46257 ± 0.00003	18.86112 ± 0.00076
e	⋯	0.00000	0.08329	0.00089 ± 0.00065	0.08220 ± 0.00473
ω	deg	89.79621	216.71379	61.89388 ± 36.98216	215.56678 ± 1.90214
M_0	deg	0.00000	0.00032	27.96061 ± 20.80132	1.12536 ± 0.80464
i	deg	89.50262	88.99146	89.51412 ± 0.31257	88.95986 ± 0.51613
Ω	deg	0.00000	0.00006	185.70005 ± 116.59810	184.90569 ± 116.58777
$-\ln \mathcal{L}$	⋯	−61.93923		−74.96317	
χ^2	⋯	428		455	
$\chi^2_{\rm red}$	⋯	36		38	
ΔAICc	⋯	−57.69664		−83.74452	

et al. 2017; Foreman-Mackey 2018)[62] and use the sum of two `SHO` kernels, where only one of the frequencies is a free hyperparameter, and the other is fixed to its first harmonic. Both oscillators are forced by a lower boundary of the quality factor to be in the underdamped regime (i.e., $Q > 1/2$). For the RV data and the TESS light curves, the same rotation period and quality factors are enforced; however, the variance can differ.

We performed the photodynamical modeling in two versions. In the first (model A, using 45,000 steps after 10,000 burn-in steps and 400 walkers), we simultaneously fit the flares in the TESS light curves using the flare model `aflare` (Davenport et al. 2014). In the second version (model B, using 10,000 steps after 10,000 burn-in steps and 100 walkers; will be increased), we use the cleaned TESS light curve from Gilbert et al. (2022), where the variation due to stellar activity has also been corrected; i.e., no GP modeling is required here for the transit light curves. The parameters of the photodynamical fits are listed in Table 20 and displayed in Figures B1 and B2.

[62] https://celerite2.readthedocs.io/en/latest/api/python

5.1. Photodynamical Modeling Results

In this subsection, we present a summary of the key results of our photodynamical modeling. Model A has the advantage of providing a simultaneous fit of the transits, stellar activity modulation, and flares. Since the timescales of ingress and egress are similar to those of the flares, a simultaneous fit should provide a more robust result. The flexibility of the GP kernels, however, may compensate for small deviations in time between observed and modeled transits. Comparing the calculated transit midpoints of a best fit to the a priori measured mid-transit times indeed shows deviations on the order of 10 minutes. Either the transit midpoint measurements are affected by systematic errors due to the stellar activity and flaring or the GP model is too flexible and hides these discrepancies. In model B, this is prevented due to a precleaning of the light curve but with the caveat that the measured mid-transit times may be affected by activity modulation and flaring. A comparison between the two approaches shows that we can obtain a two-planet model that fits all transits (TESS, Spitzer, and ground-based) if the stellar variability and flares are fitted simultaneously, while all models compared to the precleaned data show noticeable discrepancies. As an example, we show the first transit of AU Mic b in Sector 1 of TESS in Figure 7, in the top two panels from the simultaneous stellar

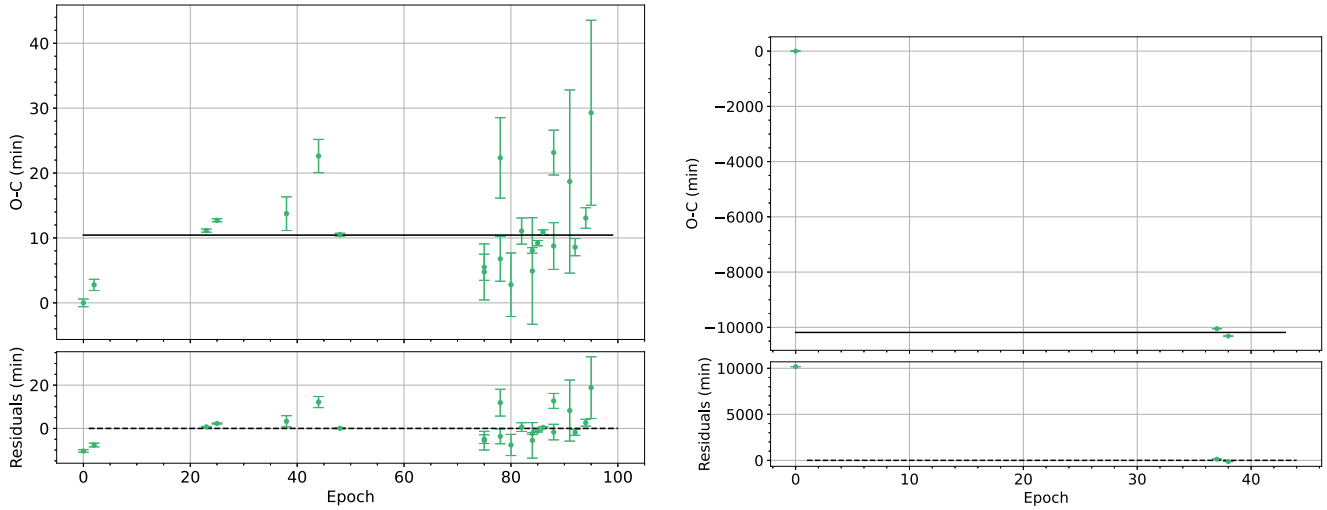

Figure 5. Massless planets $O - C$ diagram of AU Mic b (left) and AU Mic c (right), with comparison between TTVs (green) and `Exo-Striker`-generated best-fit models (black).

Table 17
`Exo-Striker`-generated Parameters for AU Mic Massless Planets Best-fit and MCMC Modeling

Parameter	Unit	Best-fit		MCMC	
		AU Mic b	AU Mic c	AU Mic b	AU Mic c
K	m s^{-1}	0.00000	0.00000	0.00000 ± 0.00000	0.00000 ± 0.00000
$P_{\rm orb}$	day	8.46293	19.04753	8.46293 ± 0.00000	18.98613 ± 0.00002
e	⋯	0.00004	0.00001	0.47442 ± 0.09381	0.37308 ± 0.00000
ω	deg	223.78788	0.00007	230.38681 ± 18.24298	0.00000 ± 0.00000
M_0	deg	225.89190	0.00010	193.13783 ± 7.76425	0.00000 ± 0.00000
i	deg	90.73560	88.59738	89.47176 ± 0.29016	69.69803 ± 0.00001
Ω	deg	0.00002	0.00000	189.38073 ± 126.18823	180.59530 ± 125.12807
$-\ln \mathcal{L}$	⋯	−20,683,716.47978		−6,083,619,013.93697	
χ^2	⋯	41,367,738		12,167,264,028	
$\chi^2_{\rm red}$	⋯	2,954,838		869,090,288	
ΔAICc	⋯	−41,367,384.95956		−12,167,237,979.87394	

Table 18
`Exo-Striker`-generated Parameters for AU Mic Three-planet Best-fit and MCMC Modeling

Parameter	Unit	Best-fit			MCMC		
		AU Mic b	AU Mic c	AU Mic d	AU Mic b	AU Mic c	AU Mic d
K	m s^{-1}	17.40198	7.65369	5.07363	1.91815 ± 1.27252	9.21910 ± 0.50712	1.06232 ± 0.30432
$P_{\rm orb}$	day	8.46340	18.85872	13.48517	8.46329 ± 0.00027	18.86224 ± 0.00126	13.46591 ± 0.01022
e	⋯	0.02348	0.00000	0.00000	0.07436 ± 0.00994	0.02508 ± 0.01531	0.00998 ± 0.00752
ω	deg	89.96574	223.91754	70.01180	85.48567 ± 6.11803	210.12425 ± 16.99204	43.40723 ± 31.78809
M_0	deg	0.00000	0.00000	0.00000	5.18482 ± 3.84571	11.58305 ± 8.87570	42.36104 ± 29.98678
i	deg	89.47231	89.10159	115.68159	89.43632 ± 0.30223	88.99503 ± 0.54176	103.58128 ± 4.14661
Ω	deg	0.00000	0.17063	0.00000	123.30784 ± 87.12008	162.09943 ± 91.36624	139.42421 ± 90.81975
$-\ln \mathcal{L}$	⋯		73.34798			−848.73127	
χ^2	⋯		158			1991	
$\chi^2_{\rm red}$	⋯		32			398	
ΔAICc	⋯		419.69596			−1424.46254	

variability and flare fit and the bottom panel from the precleaned data. We also show the best fit for one of the Spitzer light curves in Figures 8 and 9.

While the best fit of the photodynamical model including stellar variability and flares is promising, we note the abovementioned compensation of deviations between models

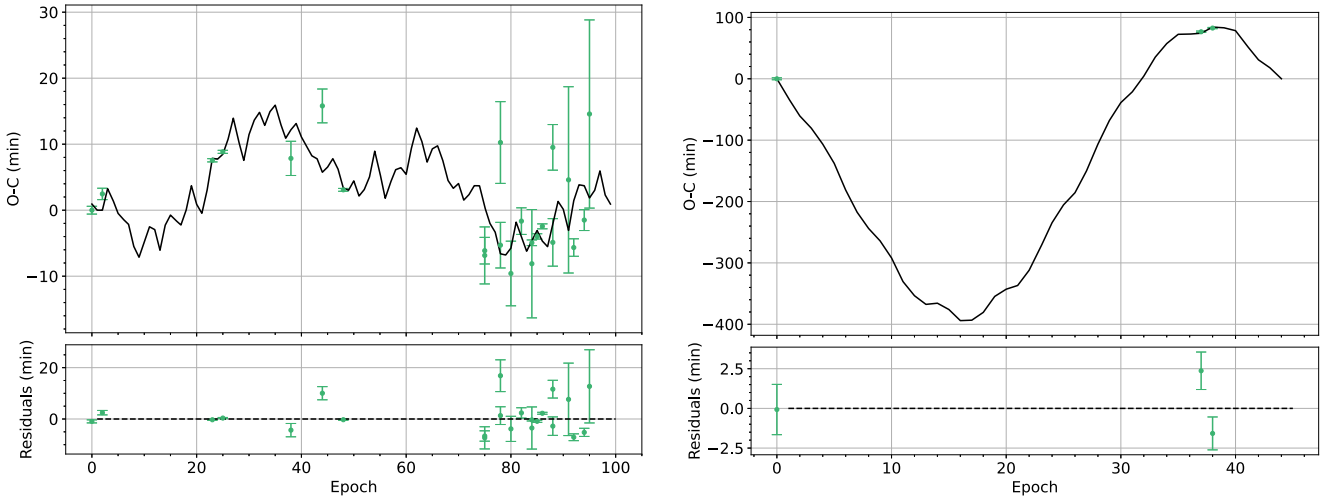

Figure 6. Three-planet $O - C$ diagram of AU Mic b (left) and AU Mic c (right), with comparison between TTVs (green) and `Exo-Striker`-generated best-fit models (black).

Table 19
Comparisons of Best-fit Model Fitting Parameters among the Massless Planets, Two-planet, and Three-planet Cases

Best-fit Model	χ^2	$\chi^2_{\rm red}$	$-\ln \mathcal{L}$	ΔAICc
No TTVs	41,367,738	2,954,838	−20,683,716.480	−41,367,384.960
Two-planet	428	36	−61.939	−57.697
Three-planet	158	32	73.348	419.696

Table 20
Parameters for the Photodynamical Models, with Model A the Simultaneous Fit of Stellar Activity Variation and Flares and Model B the Precleaned Data

Parameter	Unit	Model A		Model B	
		AU Mic b	AU Mic c	AU Mic b	AU Mic c
$M_{\rm p}$	$M_\oplus$	16^{+12}_{-9}	$10.8^{+2.3}_{-2.2}$	13^{+8}_{-2}	13^{+5}_{-2}
Period	days	$8.4626^{+0.0001}_{-0.0001}$	$18.8624^{+0.0015}_{-0.0011}$	$8.4626^{+0.0001}_{-0.0002}$	$18.860^{+0.002}_{-0.002}$
Eccentricity	⋯	$0.022^{+0.005}_{-0.006}$	$0.097^{+0.010}_{-0.013}$	$0.012^{+0.003}_{-0.003}$	$0.069^{+0.025}_{-0.014}$
ω	deg	84^{+7}_{-9}	$99.1^{+3.7}_{-3.5}$	103^{+6}_{-7}	112^{+5}_{-9}
$t_{\rm peri}$	days	$4.87^{+0.16}_{-0.21}$	$4.89^{+0.15}_{-0.16}$	$5.3^{+0.2}_{-0.2}$	$5.5^{+0.2}_{-0.4}$
$R_{\rm p}/R_\star$	⋯	$0.0529^{+0.0002}_{-0.0002}$	$0.032^{+0.002}_{-0.001}$	$0.0511^{+0.0002}_{-0.0001}$	$0.034^{+0.006}_{-0.001}$
Inclination	deg	$89.20^{+0.06}_{-0.06}$	$90.8^{+0.1}_{-0.1}$	$89.11^{+0.03}_{-0.03}$	$89.4^{+0.08}_{-0.07}$

Note. Orbital elements are given for BJD 2,458,300.

and observation due to the flexibility of the GP model. Further transits will be required to check this model. The timing discrepancies in the second version of the photodynamical fit corroborate the conclusion from our TTV fitting (i.e., a two-planet model is not able to reproduce the small but detectable TTVs).

6. Discussion

In this section, we present the key results of our analyses in Section 6.1, followed by the impact of the rotational modulation of stellar spots and plages in Section 6.2 and flares in Section 6.3. In Section 6.4, we assess the likelihood of an additional middle nontransiting planet candidate to explain the observed TTVs, and in Section 6.5, we compare our analyses' constraints on the mass of AU Mic c. Lastly, in Section 6.6, we discuss the limitation of our joint modeling.

6.1. Key Results of Analyses

In the preceding sections, we modeled the transit observations of AU Mic b and c to ascertain whether or not TTVs were present, as well as whether or not they can be accounted for by our existing knowledge of this planetary system and used to constrain the dynamical orbits and masses of the two transiting planets. Given the inherent stellar activity in this young system, we explored two different and independent analyses: in Section 4, a dynamical model of the transit midpoint times, and in Section 5, a full photodynamical model. We found in both scenarios indications of TTVs deviating from a linear ephemeris on the order of 10 minutes, particularly when

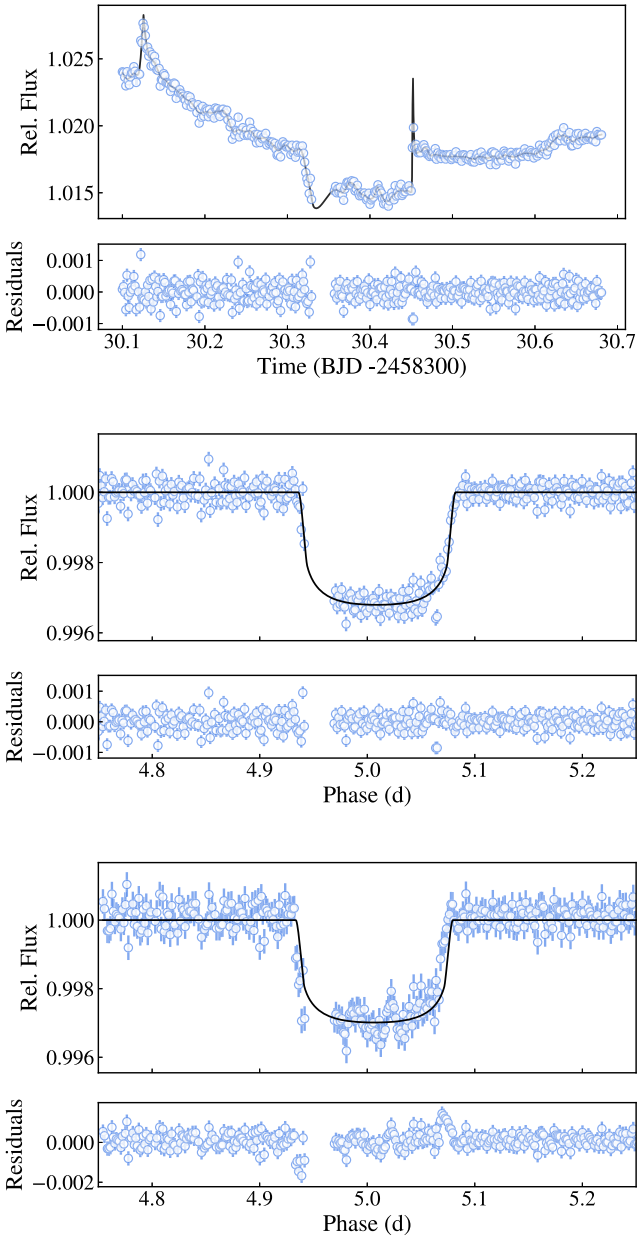

Figure 7. First TESS transit of AU Mic b in Sector 1. From top to bottom: TESS light curve with stellar activity variation and flares overlaid with the best-fit model A from the photodynamical analysis, the best-fit model A with the contribution of stellar activity variation and flares removed, and the best-fit model B.

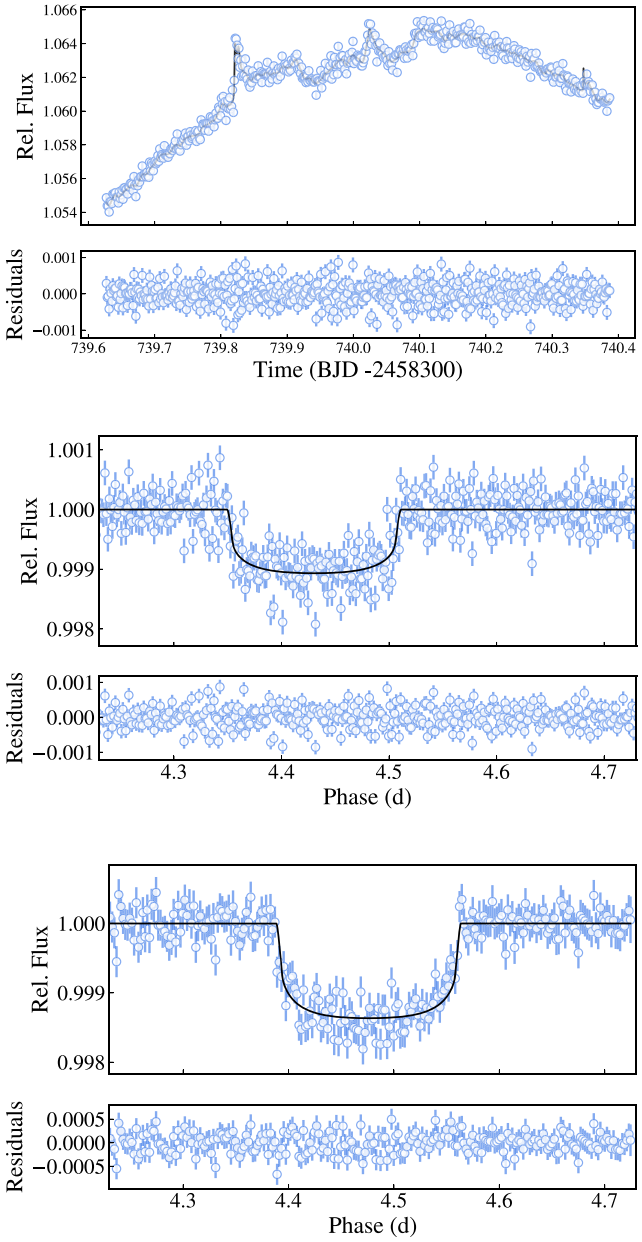

Figure 8. First TESS transit of AU Mic c in Sector 27. From top to bottom: TESS light curve with stellar activity variation and flares overlaid with the best-fit model A from the photodynamical analysis, the best-fit model A with the contribution of stellar activity variation and flares removed, and the best-fit model B, which shows by eye a clear timing offset when the activity is modeled separately from the photodynamical modeling.

comparing the TESS and Spitzer transit times, and generally consistent results, albeit with larger timing uncertainties, from the ground-based transits and R-M observations (Figure 3).

We next explored whether the two transiting planets could account for the observed TTVs. We first attempted a two-planet dynamical model for the TTVs with only the high-precision TESS transits, for which we were able to find a fit akin to that derived in Martioli et al. (2021). These transit times were derived with the joint stellar activity model in Gilbert et al. (2022), who found evidence for TTVs on the order of a few minutes. However, when including the Spitzer transits, which are less susceptible to stellar activity at 4.5 μm, we find that the Spitzer transits are incompatible with this model within the measured timing uncertainties, showing a significant departure from a circular two-planet model on the order of $\sim$10 minutes. We next considered whether orbital eccentricity could account for the observed TTVs but derive high eccentricities that are incompatible with the light curves themselves, which exclude high-eccentricity scenarios (Plavchan et al. 2020; Gilbert et al. 2022).

With the full photodynamical analysis in Section 5, we were able to jointly model the activity and transits to reproduce the observed transit midpoint times. However, this left open the possibility that the flexibility of the GP for the rotational modulation of the starspots could also absorb any of the TTVs present. In fact, with a second photodynamical model using the Gilbert et al. (2022) activity model with detrended transit light curves (e.g., the stellar activity is corrected serially rather than

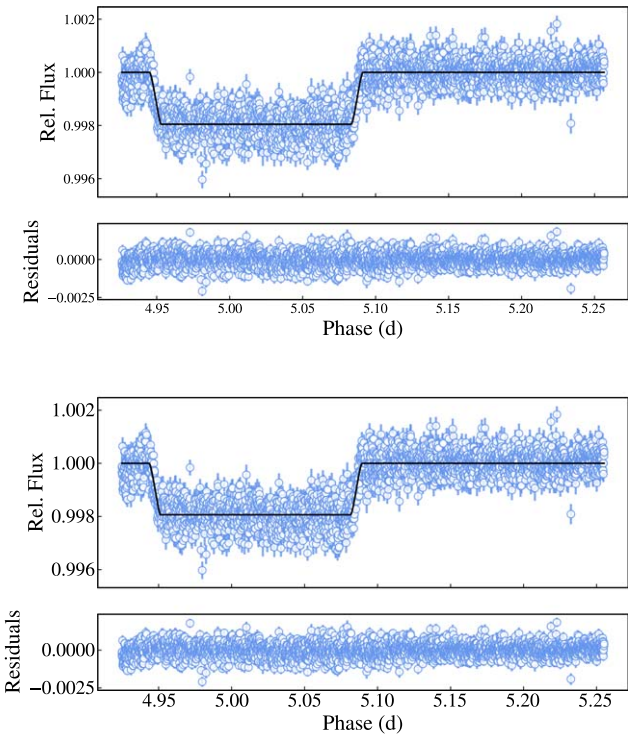

Figure 9. First Spitzer transit of AU Mic b, with the best-fit model A (top) and B (bottom) from the photodynamical analysis.

jointly with the photodynamical analysis), we found excess TTVs not explained by the two-planet model alone.

In order to explain the observed excess of TTVs accounted for by our two-planet modeling, we next investigate the following possibilities. First, we consider whether our modeling of the rotational modulation of starspots is underestimating the impact on the TTVs. Second, we consider the impact the flares have on our TTVs. Third, we consider the possibility of a third planet in the AU Mic system not yet detected through the transit or RV method. Finally, we consider the limitations of our analysis and statistical methods.

6.2. Stellar Spots

Stellar spots can significantly impact the recovered stellar and planetary model parameters (Pont et al. 2007; Czesla et al. 2009; Berta et al. 2011; Désert et al. 2011; Ballerini et al. 2012) and produce TTV-like signals that potentially lead to false-positive detections of nontransiting planets (Alonso et al. 2009; Sanchis-Ojeda et al. 2011; Sanchis-Ojeda & Winn 2011; Oshagh et al. 2012). For $R_p/R_\star \approx 0.05$ (as is the case for AU Mic b), the expected maximum amplitude of the spot-induced TTV in seconds at visible wavelengths is $\mathrm{AMP} = 139 \times f$, where f is the stellar spot-filling factor in percent (Oshagh et al. 2013). If $f = 0.25\%$, 1%, or 3%, the maximum amplitude would be 34.75, 139, or 417 s (0.6, 2.3, or 7.0 minutes), respectively. Given the long-lived spot lifetimes for AU Mic, it is not unreasonable to assume that the spot-filling fraction is >3%; thus, the impact of the rotational modulation of starspots could be on the order of >7 minutes. Oshagh et al. (2013) added that if the transit duration and depth priors were fixed (and not modeled), the TTV amplitude would be smaller than if they were floating.

Table 21
Weighted Averages of the Respective Initial, Two-planet Model-subtracted, and Three-planet Model-subtracted TTVs as a Function of Transit Number Modulo 4

Phase	TTV_i (minutes)	TTV_2 (minutes)	TTV_3 (minutes)
1	0.52 ± 1.17	-0.90 ± 0.59	-0.40 ± 0.59
2	4.61 ± 1.00	1.11 ± 0.52	0.06 ± 0.52
3	0.99 ± 1.28	0.61 ± 0.79	1.88 ± 0.79
4	4.89 ± 1.13	-0.36 ± 0.54	-0.40 ± 0.54

First, we consider the wavelength dependence of the TTVs. The Spitzer transit times have greater photometric precision due a larger aperture, a much higher cadence, and consequently more precise transit midpoint times (to within 13 s). Further, the Spitzer observations are less impacted by the rotational modulation of stellar activity at 4.5 μm due to the decreased flux contrast of any spots; the rotational modulation of stellar activity should be significantly decreased in amplitude. This decreased amplitude of the impacts of stellar activity with increasing wavelength is also observed for AU Mic in photometry (Hebb et al. 2007) and RVs (Cale et al. 2021). However, the Spitzer transits show more significant deviations from a linear ephemeris than those derived by the TESS data alone, running counterintuitive to the expected impact the rotational modulation of starspots would have on the derived transit times.

Second, Szabó et al. (2021) measured AU Mic's rotation period with TESS data and AU Mic b's orbital period with both TESS and CHEOPS light curves and found that the ratio between these two periods implies the 7:4 spin–orbit commensurability. Due to this resonance, for every fourth transit of AU Mic b, the transit takes place over the same range of stellar longitudes of AU Mic. In other words, the same stellar "side" is transited every fourth transit. Thus, the impact of the stellar rotational modulation of spots should produce the same systematic impact on the TTVs every fourth transit. For example, if the first transit of AU Mic b is 4 minutes "late" from the apparent effects of starspots, then this will also be true for the 5th, 9th, 13th, 17th, …, Nth transits. Given AU Mic's long spot lifetime, relatively unchanged between TESS Sectors 1 and 27 2 yr later, this pattern will have persisted over the duration of our observations.

To explore the impact of spot modulations on TTVs, we calculated the weighted average of the initial two- and three-planet model TTVs for each of the four phases (Table 21); from there, we can see correlations between phases 1 and 3 and phases 2 and 4. However, after subtracting the two- and three-planet models from the respective TTVs, these correlations disappeared. Thus, no such "modulo 4" pattern is observed in the AU Mic b transit times (Figure 10), with the transits being neither systematically late nor early in phase with the stellar longitude crossings. The three Spitzer transits are from three different sets of stellar longitude crossings, and one of the R-M observation midpoint times is from the fourth set of stellar longitude crossings; all four transit midpoint times are systematically late with regard to the TESS transit times by ~5–10 minutes. The TESS transits themselves also encompass three of the four stellar longitude crossing sets, and the variation in transit times between them is less than a couple of minutes.

Third, Gilbert et al. (2022), in deriving the TESS transit midpoint times, included the joint modeling of the rotational

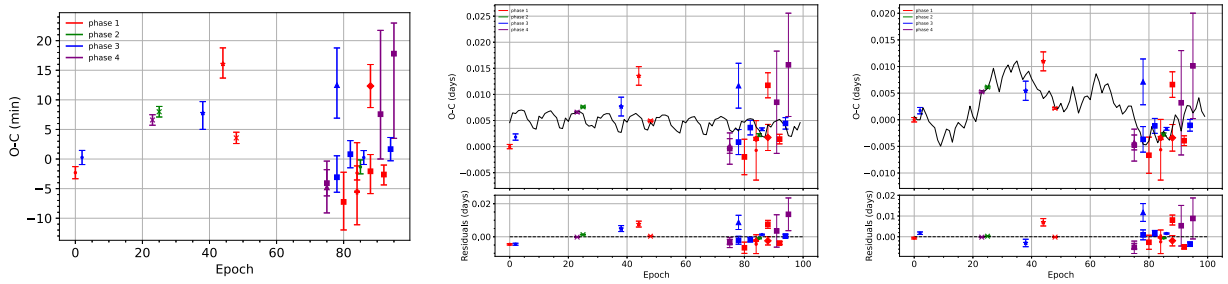

Figure 10. The $O-C$ diagram of AU Mic b from the initial model (left), `Exo-Striker` two-planet model (middle), and `Exo-Striker` three-planet model (right), color-coded as a function of transit number modulo 4, using the `EXOFASTv2`-generated measured midpoint times and the calculated midpoint times for all 23 AU Mic b transit data sets from Table 3. Here we explore the impact the rotational modulation of starspots, given the 7:4 spin–orbit commensurability, may have on the observed TTVs. The weighted averages of the distribution of TTVs for each of the four stellar longitude crossing phases are in Table 21; they show correlations between phases 1 and 3 and phases 2 and 4. However, after subtracting the two- and three-planet models from the TTV data, the weighted averages show no clear correlation of more than ∼2 minutes, indicating that the stellar spots of AU Mic are not a significant factor in accounting for the timing of transits for AU Mic b. The epochs are relative to the first TESS transit of AU Mic b.

modulation of the starspots in deriving the transit midpoint times. This analysis approach thus mitigates any impact the spot modulation has on the values of the derived transit midpoint times as estimated in Oshagh et al. (2013). Additionally, because of the joint modeling of the TESS transits, the impact of the rotational modulation is reflected in the posterior uncertainties and thus precision in the derived transit times. Our photodynamical analysis has shown that when modeling the rotational modulation of starspots with a GP in parallel with deriving transit midpoint times, as opposed to in series, the GP can absorb rather than introduce additional TTVs on the order of a few minutes for AU Mic.

Thus, in light of the modeling presented herein and Gilbert et al. (2022), the rotational modulation of starspots can likely be ruled out as an explanation for our observed TTVs between TESS and Spitzer. More detailed synthetic simulations will be needed in the future to further quantify the impact of the rotational modulation of AU Mic starspots on the derived transit times, but that is beyond the scope of this work. We next turn to assessing the impact of flares on the derived transit times.

6.3. Stellar Flares

Like stellar spots, stellar flares can impact the midpoint timing of the transits, particularly when they occur during ingress or egress, which happened several times during the TESS transits. For the ground-based transit data, it is difficult to resolve the flares due to the relatively lower photometric precision; additionally, `AIJ` and `EXOFASTv2` do not include joint modeling of flares during transits. The ground-based transit times also possess larger timing uncertainties, which may mask the impact of flares.

Several flares occurred during the TESS observations, but Gilbert et al. (2022) jointly modeled them with the `bayesflare` (Pitkin et al. 2014) and `xoflares` packages, some of which do occur during egress and thus could impact the derived transit midpoint times were they not modeled jointly. Additionally, the $O-C$ diagram from our photodynamical analysis demonstrates that the derived transit times are sensitive to the methods employed for accounting for the stellar flares. However, the analysis done by Gilbert et al. (2022) shows no dependence of transit timing on activity after marginalizing over models for the flares and spot modulation, and the TESS transit times of AU Mic b are fairly constant to within ∼4 minutes.

The second partial Spitzer transit of AU Mic b contains an obvious flare during transit, which we marginalize over in our modeling, thus impacting our derived timing uncertainties. Additionally, the first and third Spitzer transits may show some small flares pre-ingress, which we do not account for in our modeling. As with spots, however, flares are smaller in amplitude at 4.5 μm than at visible wavelengths and thus should have a relatively smaller impact on the derived transit times. However, we find that the first two Spitzer transit times are consistent with one another, and the third Spitzer transit is most contemporaneous with the R-M transit observations.

For the SPIRou + iSHELL R-M transit observation, the analysis took into account the impact of magnetic activity and flares by constructing a model using a similar approach from Donati et al. (2020), which is then subtracted from the RV observations. Similarly, for the ESPRESSO data, the stellar activity was modeled using the `celerite` package's GP that is described by a Matérn 3/2 kernel and then subtracted from the RV data.

All five R-M and Spitzer transits show significantly deviant and late transit times. It would be difficult and randomly unlucky to have randomly timed flares during the different transits all impact the derived transit midpoint times in the same way: late, as opposed to early. While these results are based on a relatively small number of transits, it seems unlikely that flares can account for the observed TTV excesses. More detailed simulations in the future will be needed to assess the impact of flares on the transit times of AU Mic, but that is beyond the scope of this work. We next turn to considering the possibility of additional planets in the AU Mic system.

6.4. Existence of a Planet d Candidate?

In the previous subsections, we explored the stellar activity of AU Mic and the significance of its impact on the TTVs, through the rotational modulation of starspots and through flares. It is possible that there is some unaccounted-for effect in the derived TTV uncertainties, but we deem this scenario unlikely given the above marginalization over our activity models in the derived transit time posteriors. Thus, we turn to another possibility: the presence of a third planet.

Cale et al. (2021) explored additional candidate RV planet signals when modeling the RVs of the AU Mic system. One candidate period that was explored in particular was the presence of a planet in between b and c, a "middle-d" nontransiting planet with a period of 12.742 days. Such a planet

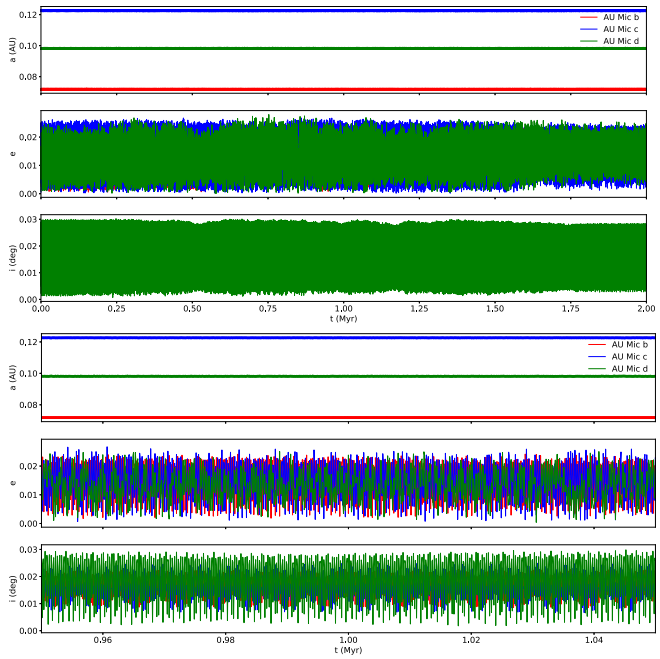

Figure 11. . A `rebound` model of the stability of a three-planet system for AU Mic. The top three plots span 2 Myr, while the bottom three plots are zoomed in between 0.95 and 1.05 Myr.

would establish that the AU Mic system is in a 4:6:9 orbital commensurability and result in significant TTVs. In Section 4.2.2, we modeled this three-planet configuration with `Exo-Striker` based on this candidate RV signal from Cale et al. (2021). Since the AMD criterion indicated that this configuration is unstable, we tested its stability with *N*-body packages, including `rebound` (Rein & Liu 2012; Rein & Spiegel 2015) and `mercury6` (Chambers 1999), the latter of which was used as a consistency check. The `mercury6` simulation ran for 10 Myr, while the `rebound` simulation ran for 2 Myr; both indicated that the three-planet configuration from Section 4.2.2 is stable (see Figure 11 for outputs from `rebound`). Additional possible configurations, including having a planet beyond c, is beyond the scope of this work. While we find that our TTVs are consistent with a possible third "middle-d" transiting planet, we neither confirm nor rule out its existence. If this third planet does exist, our dynamical modeling implies that the impact on the observed TTVs will be more readily apparent with additional TTV measurements in 2021 and the next several years, as the TTVs for AU Mic b would deviate further from a linear ephemeride, and given the "curvature" in the TTVs from the first 3 yr of TTVs presented herein.

6.5. Implication for the Mass of AU Mic c

With only three transits of AU Mic c, all with relatively larger transit timing uncertainties, we do not derive a TTV mass constraint for AU Mic b. However, from the perturbations of the transit times of AU Mic b, we are able to place constraints on the mass of AU Mic c. Table 22 summarizes our `Exo-Striker` and photodynamical TTV masses with the RV masses from Cale et al. (2021). In both our two- and three-planet `Exo-Striker` models, the mass of AU Mic c is approximately that of Neptune. Both photodynamical models determine the mass of AU Mic c to be more comparable to that of Uranus than the more massive Neptune. The densities of AU Mic c using the masses from `Exo-Striker` analyses are quite high. We instead adopt as our final mass estimate for AU Mic c $10.8^{+2.3}_{-2.2}$ $M_\oplus$, the value from our A photodynamical model, which jointly models the stellar activity with the transit dynamics with no third planet. This value is consistent with the mass for AU Mic c as determined from RVs (as are all of the masses we derive). Note that we only list the masses of AU Mic c; we currently do not have enough transits or precision on the timing of transits for AU Mic c to place a meaningful constraint on the mass of AU Mic b.

Table 22
Characteristics of AU Mic c

Property	Unit	Quantity	References
Mass	$M_\oplus$	$9.60^{+2.07}_{-2.31}$	K_{J1} (Cale et al. 2021)
		$14.12^{+2.48}_{-2.71}$	K_{J2} (Cale et al. 2021)
		24.8 ± 1.2	`Exo-Striker` two-planet model
		20.1 ± 1.6	`Exo-Striker` three-planet model
		$10.8^{+2.3}_{-2.2}$	Photodynamical model A
		13^{+5}_{-2}	Photodynamical model B
Radius	$R_\oplus$	$2.79^{+0.31}_{-0.30}$	Gilbert et al. (2022)
Density	g cm^{-3}	$2.44^{+0.97}_{-0.98}$	K_{J1} (Cale et al. 2021)
		3.58 ± 1.35	K_{J2} (Cale et al. 2021)
		$6.28^{+2.12}_{-2.05}$	`Exo-Striker` two-planet model
		$5.08^{+1.74}_{-1.69}$	`Exo-Striker` three-planet model
		$2.75^{+1.09}_{-1.05}$	Photodynamical model A
		$3.3^{+1.7}_{-1.2}$	Photodynamical model B

6.6. Limitation of Our Joint Modeling and Future Work

In this subsection, we discuss some of the limitations of our analysis. First, we do not perform joint RV + TTV modeling because the RVs require a custom treatment of stellar activity that is an order of magnitude larger in effective amplitude relative to the Keplerian orbital reflex motion of the star (Cale et al. 2021). We also sought to conduct an independent TTV modeling to compare with the RV analysis, given the complexity of the RV model. Additionally, to our knowledge, no prior work exists in performing a joint RV + TTV modeling in the presence of such stellar activity as exhibited by AU Mic.

Second, in RVs, it is common to adopt a jitter term representing the white-noise measurement error that is not captured by the formal measurement uncertainties and added in quadrature, without which Keplerian orbital fits can yield a reduced $\chi^2 \gg 1$. A similar approach may be employed for AU Mic in a future study for the TTV modeling, including a jitter term that accounts for timing uncertainties not captured by our modeling of spots, flares, and orbital dynamics. We do not undertake such an analysis herein for several reasons. First, `Exo-Striker` does not include a jitter TTV error term, and thus we cannot marginalize over this parameter; e.g., we would need to assume a jitter timing term and inflate our timing measurement uncertainties. Second, our timing data are fairly inhomogeneous, spanning a range of precision and wavelength from ground and space facilities; we would need multiple independent jitter terms that are not well constrained, and our Spitzer data that most deviate from a two-planet TTV model are least impacted by stellar activity. Third, as shown in Szabó et al. (2021), due to the 7:4 period commensurability of the stellar rotation to the orbital period of AU Mic b, the TTV jitter

from spots will not be a white-noise term; given the known stellar rotation period, the timing impact is not simply random and fairly deterministic, as we have undertaken our "mod-4" transit analysis to identify whether or not the transit times correlate with the stellar longitude crossings. That being said, the flares are random in time and will randomly impact the measured transit times. Therefore, a jitter term would be appropriate for accounting for the impact of flares on the measured TTVs that are not captured by our flare modeling of the light curves.

Third, the uncertainties in the midpoint times from the R-M observations are likely to be underestimated. As allowing certain parameters, such as the orbital period and eccentricity, to remain free will result in degeneracy in the R-M model, setting such parameters fixed would avoid this issue but cause the uncertainties to be underestimated.

As a consequence of these limitations in our analysis, we do not perform any statistically robust model comparisons between the two- and three-planet TTV models. Future observations and analyses will be necessary to reach a definitive conclusion for the hypothetical third planet candidate.

7. Conclusion

Star AU Mic hosts a young nearby exoplanet system that serves as a useful laboratory for probing and characterizing young exoplanetary systems. We have collected 23 transits from AU Mic b and three transits from AU Mic c over the course of 3 yr. We model the observed transits and derive new transit model posteriors. We have run two independent methods (`Exo-Striker` and photodynamical) in modeling the transits and the timing of those transits. Our observations and analyses of the transits of AU Mic b and c show that AU Mic b is exhibiting TTVs, consistent with Szabó et al. (2021), Martioli et al. (2021), and Gilbert et al. (2022). Our photodynamical model yields a mass for AU Mic c of $10.8^{+2.3}_{-2.2}$ $M_{\oplus}$, consistent with the RV-determined mass in Cale et al. (2021). However, going beyond the work of Szabó et al. (2021) and Martioli et al. (2021), our TTVs show a timing excess of >5 minutes that appears discrepant with a two-planet model alone, particularly when comparing the Spitzer and TESS derived transit times, the former of which is presented for the first time herein. Further, we marginalize our TTV models over our models for the rotational modulation of stellar activity and flares. Consequently, stellar activity, while not excluded through statistically robust model comparison, does not appear likely to be able to account for the observed TTV excess. We mapped the $O-C$ diagram, taking into account AU Mic's stellar spin 7:4 commensurability with the orbital period of AU Mic b from Szabó et al. (2021), and we did not identify that the spot modulation results in a significant effect on the observed TTVs as a function of stellar longitude crossings. We explore a possible, representative, and nonexhaustive three-planet configuration scenario that is consistent with the identified nontransiting "middle-d" RV candidate signal in Cale et al. (2021), is dynamically stable, would establish the AU Mic system of planets in a 4:6:9 orbital period commensurability, and can account for the observed TTV excess of our data.

Nonetheless, given the high level of stellar activity for AU Mic, we cannot ignore the possibility that our modeling and marginalization over our stellar activity models do not fully account for some effects that significantly impact the observed TTVs. Thus, additional ground- and space-based TTVs in the next few years are needed to further vet the impact of stellar activity on the observed TTVs, confirm the possibility that the excess TTVs are due to the RV candidate highlighted in Cale et al. (2021), and enable a more thorough search of the possible orbital periods for possible additional planets in the AU Mic system. Such observations will be possible from the ground with CHEOPS now or with upcoming missions, such as the Pandora and Twinkle missions, Ariel, and/or the James Webb Space Telescope.

P.P.P. acknowledges support from NASA (Exoplanet Research Program award No. 80NSSC20K0251, TESS Cycle 3 Guest Investigator Program award No. 80NSSC21K0349, JPL Research and Technology Development, and Keck Observatory Data Analysis), the NSF (Astronomy and Astrophysics grant Nos. 1716202 and 2006517), and the Mt. Cuba Astronomical Foundation. D.D. acknowledges support from the TESS Guest Investigator Program grant No. 80NSSC21K0108 and NASA Exoplanet Research Program grant No. 18-2XRP18_2-0136. E.G. acknowledges support from NASA Exoplanet Research Program award No. 80NSSC20K0251. The material is based upon work supported by NASA under award No. 80GSFC21M0002. L.D.V. acknowledges funding support from the Heising-Simons Astrophysics Postdoctoral Launch Program through a grant to Vanderbilt University.

This paper includes data collected by the TESS mission that are publicly available from the Mikulski Archive for Space Telescopes (MAST). Funding for the TESS mission is provided by NASA's Science Mission directorate. Resources supporting this work were provided by the NASA High-End Computing (HEC) Program through the NASA Advanced Supercomputing (NAS) Division at Ames Research Center for the production of the SPOC data products.

This work is based in part on observations made with the Spitzer Space Telescope, which was operated by the Jet Propulsion Laboratory, California Institute of Technology, under a contract with NASA. Support for this work was provided by NASA through an award issued by JPL/Caltech. This research has made use of the NASA/IPAC Infrared Science Archive, which is funded by the National Aeronautics and Space Administration and operated by the California Institute of Technology.

This work makes use of observations from the Las Cumbres Observatory global telescope network. Part of the LCOGT telescope time was granted by NOIRLab through the Mid-Scale Innovations Program (MSIP). MSIP is funded by NSF.

This research has made use of the PEST photometry pipeline[63] by Thiam-Guan Tan. This research has made use of the NASA Exoplanet Archive and the Exoplanet Follow-up Observation Program website, both of which are operated by the California Institute of Technology, under contract with the National Aeronautics and Space Administration under the Exoplanet Exploration Program. This research has made use of the SIMBAD database, operated at CDS, Strasbourg, France. This research has made use of NASA's Astrophysics Data System Bibliographic Services. This research has made use of an online calculator that converts a list of Barycentric Julian Dates in Barycentric Dynamical Time (BJD_TDB) to JD in UT (Eastman et al. 2010).[64]

[63] http://pestobservatory.com
[64] https://astroutils.astronomy.osu.edu/time/bjd2utc.html

We also give thanks to Trifon Trifonov for his assistance in the use of the Exo-Striker package and analysis of the AU Mic system.

Facilities: Brierfield:0.36 m (Moravian G4-16000 KAF-16803), CFHT (SPIRou), ExoFOP, Exoplanet Archive, IRSA, LCOGT (SAAO:1 m and SSO:1 m; Sinistro), MAST, PEST:0.30 m (SBIG ST-8XME), Spitzer (IRAC), TESS, VLT:Antu (ESPRESSO).

Software: AstroImageJ (Collins et al. 2017), astropy (Astropy Collaboration et al. 2013, 2018), batman (Kreidberg 2015), bayesflare (Pitkin et al. 2014), celerite (Foreman-Mackey et al. 2017), celerite2 (Foreman-Mackey et al. 2017; Foreman-Mackey 2018), emcee (Foreman-Mackey et al. 2013), EXOFASTv2 (Eastman et al. 2019), exoplanet (Foreman-Mackey et al. 2021), Exo-Striker (Trifonov 2019), fleck (Morris 2020), ipython (Pérez & Granger 2007), lightkurve (Lightkurve Collaboration et al. 2018), matplotlib (Hunter 2007), mercury6 (Chambers 1999), numpy (Harris et al. 2020), rebound (Rein & Liu 2012; Rein & Spiegel 2015), scipy (Virtanen et al. 2020), TAPIR (Jensen 2013), xoflares (Gilbert et al.2022).

Appendix A
Corner Plots from Main Exo-Striker Analysis

This section highlights the corner plots that were generated by Exo-Striker. All Exo-Striker corner plots are included here.

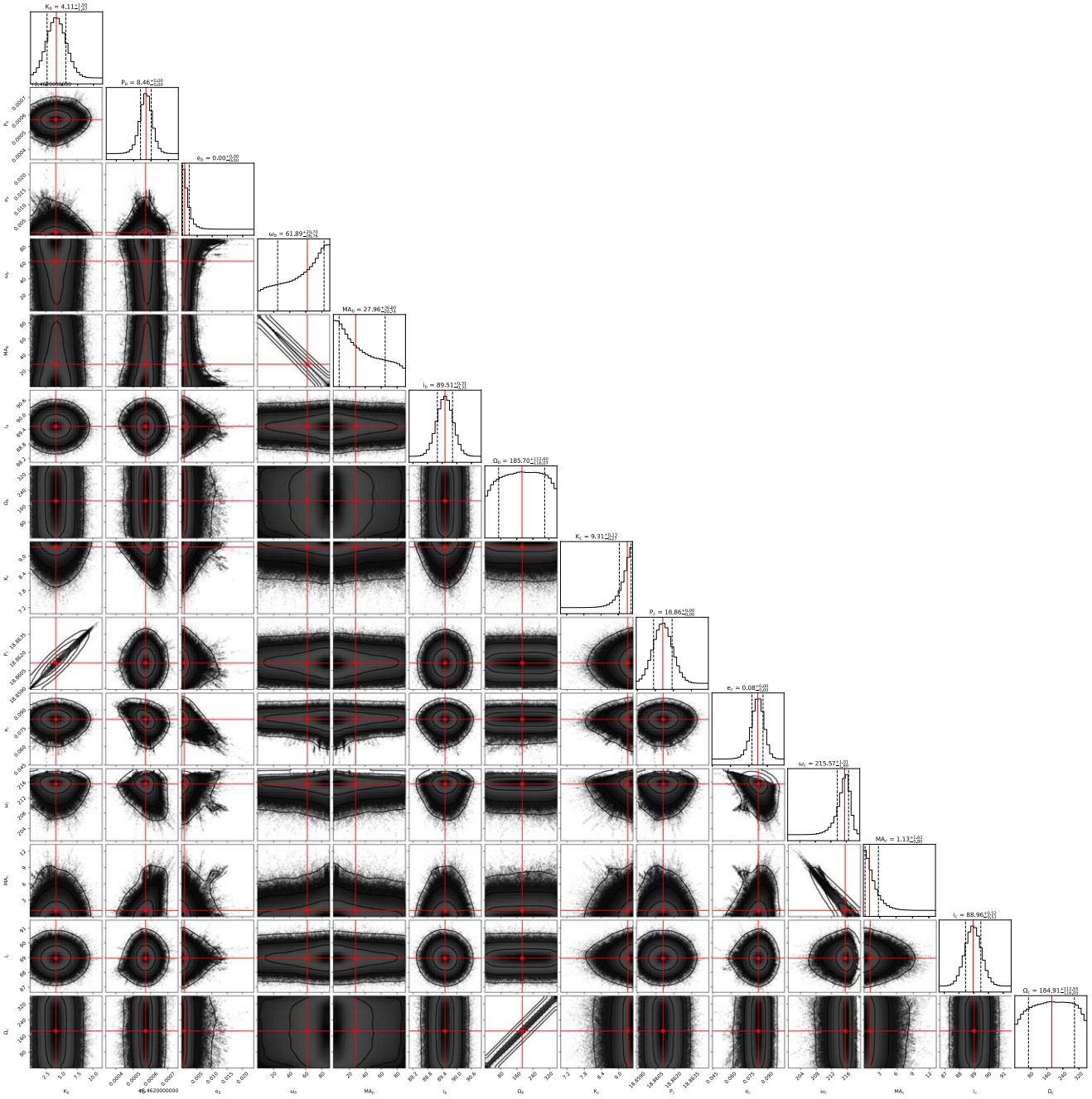

Figure A1. Exo-Striker-generated MCMC corner plot for AU Mic two-planet case. All TTVs are incorporated into this model.

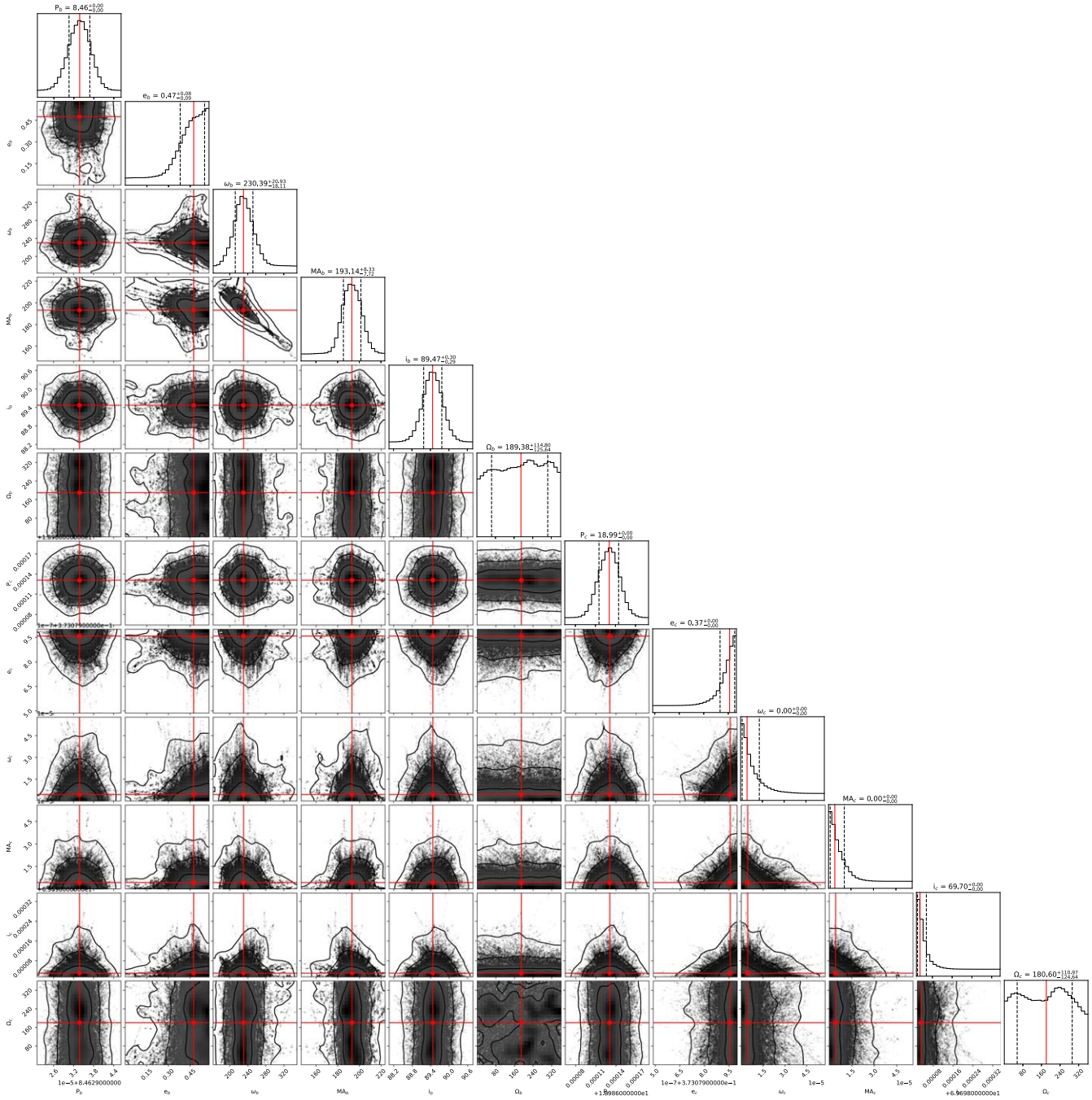

Figure A2. `Exo-Striker`-generated MCMC corner plot for AU Mic massless planets case. All TTVs are incorporated into this model.

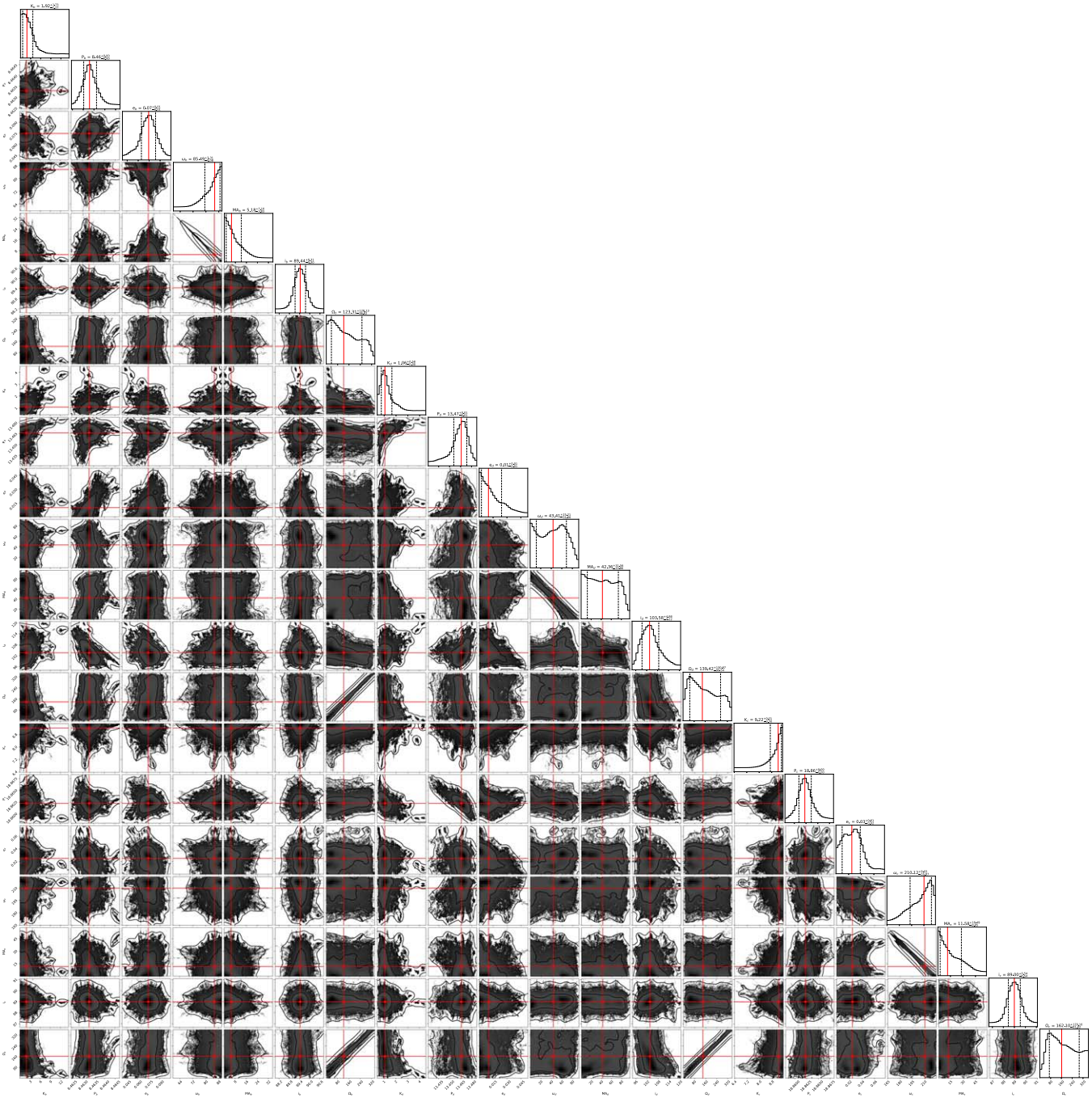

Figure A3. `Exo-Striker`-generated MCMC corner plot for AU Mic three-planet case. All TTVs are incorporated into this model.

Appendix B
Corner Plots from Photodynamical Analysis

This section highlights the corner plots that were generated by photodynamical analysis. The corner plots for both models A and B are included here.

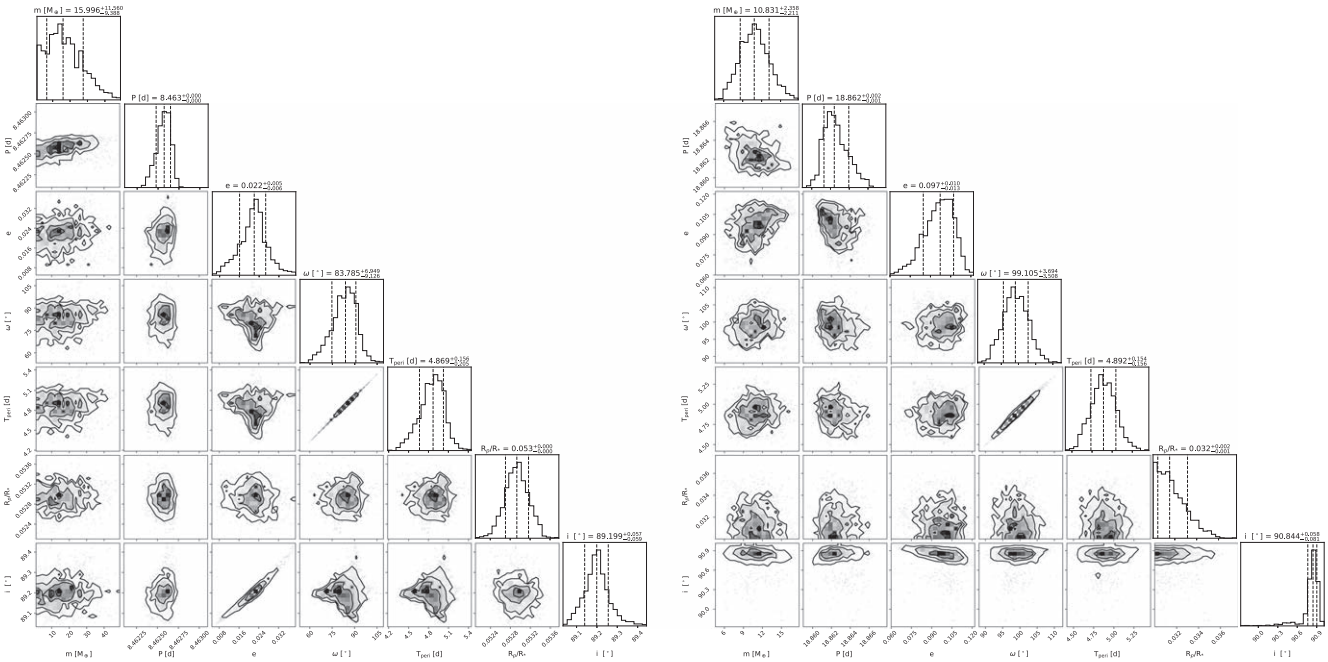

Figure B1. Corner plot for posterior distributions of orbital parameters from the photodynamical model A for AU Mic b (left) and AU Mic c (right).

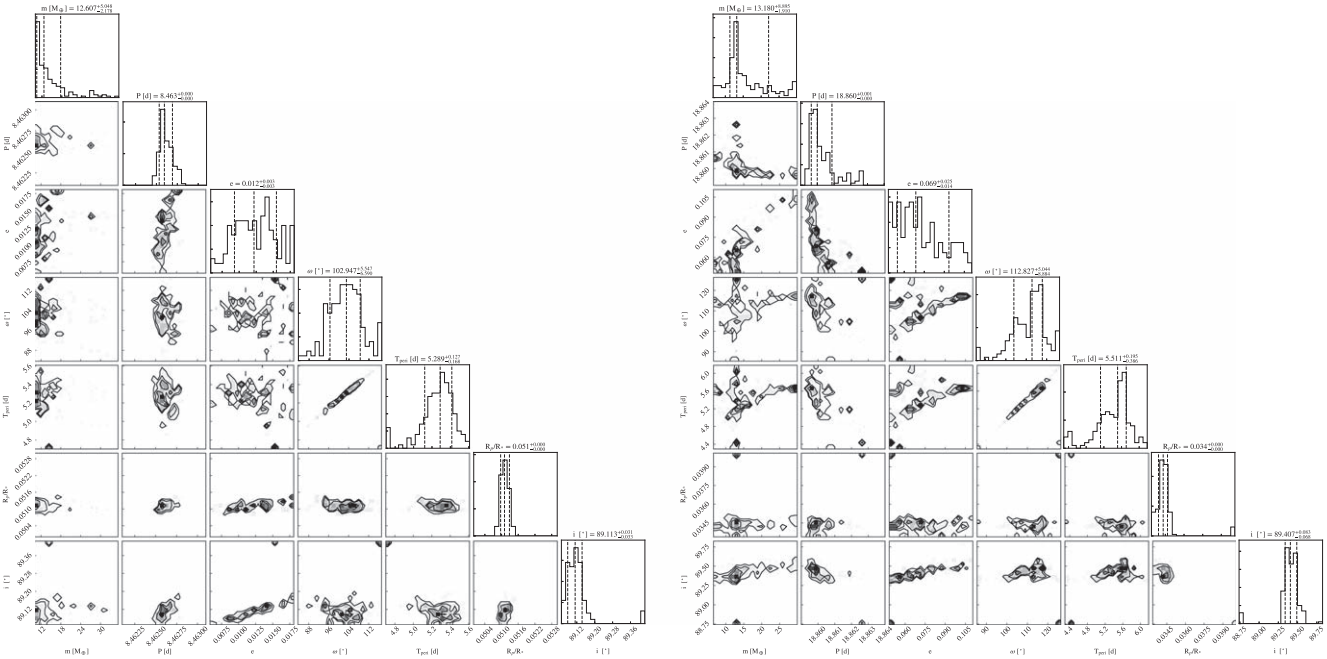

Figure B2. Corner plot for posterior distributions of orbital parameters from the photodynamical model B for AU Mic b (left) and AU Mic c (right).

ORCID iDs

Justin M. Wittrock https://orcid.org/0000-0002-7424-9891
Stefan Dreizler https://orcid.org/0000-0001-6187-5941
Michael A. Reefe https://orcid.org/0000-0003-4701-8497
Brett M. Morris https://orcid.org/0000-0003-2528-3409
Peter P. Plavchan https://orcid.org/0000-0002-8864-1667
Patrick J. Lowrance https://orcid.org/0000-0001-8014-0270
Brice-Olivier Demory https://orcid.org/0000-0002-9355-5165
James G. Ingalls https://orcid.org/0000-0003-4714-1364
Emily A. Gilbert https://orcid.org/0000-0002-0388-8004
Thomas Barclay https://orcid.org/0000-0001-7139-2724
Bryson L. Cale https://orcid.org/0000-0002-2078-6536
Karen A. Collins https://orcid.org/0000-0001-6588-9574
Kevin I. Collins https://orcid.org/0000-0003-2781-3207
Ian J. M. Crossfield https://orcid.org/0000-0002-1835-1891
Diana Dragomir https://orcid.org/0000-0003-2313-467X
Jason D. Eastman https://orcid.org/0000-0003-3773-5142
Mohammed El Mufti https://orcid.org/0000-0001-8364-2903
Dax Feliz https://orcid.org/0000-0002-2457-7889
Jonathan Gagné https://orcid.org/0000-0002-2592-9612
Eric Gaidos https://orcid.org/0000-0002-5258-6846
Peter Gao https://orcid.org/0000-0002-8518-9601
Claire S. Geneser https://orcid.org/0000-0001-9596-8820
Leslie Hebb https://orcid.org/0000-0003-1263-8637
Keith D. Horne https://orcid.org/0000-0003-1728-0304
Jon M. Jenkins https://orcid.org/0000-0002-4715-9460
Eric L. N. Jensen https://orcid.org/0000-0002-4625-7333
Stephen R. Kane https://orcid.org/0000-0002-7084-0529
Laurel Kaye https://orcid.org/0000-0002-4311-9250
Eder Martioli https://orcid.org/0000-0002-5084-168X
Teresa A. Monsue https://orcid.org/0000-0003-3896-3059
Enric Pallé https://orcid.org/0000-0003-0987-1593
Elisa V. Quintana https://orcid.org/0000-0003-1309-2904
Don J. Radford https://orcid.org/0000-0002-3940-2360
Veronica Roccatagliata https://orcid.org/0000-0002-4650-594X
Joshua E. Schlieder https://orcid.org/0000-0001-5347-7062
Richard P. Schwarz https://orcid.org/0000-0001-8227-1020
Avi Shporer https://orcid.org/0000-0002-1836-3120
Keivan G. Stassun https://orcid.org/0000-0002-3481-9052
Christopher Stockdale https://orcid.org/0000-0003-2163-1437
Thiam-Guan Tan https://orcid.org/0000-0001-5603-6895
Angelle M. Tanner https://orcid.org/0000-0002-2903-2140
Andrew Vanderburg https://orcid.org/0000-0001-7246-5438
Laura D. Vega https://orcid.org/0000-0002-5928-2685
Songhu Wang https://orcid.org/0000-0002-7846-6981

References

Addison, B. C., Horner, J., Wittenmyer, R. A., et al. 2021, AJ, 162, 137
Afram, N., & Berdyugina, S. V. 2019, A&A, 629, A83
Agol, E., Steffen, J., Sari, R., & Clarkson, W. 2005, MNRAS, 359, 567
Akeson, R. L., Chen, X., Ciardi, D., et al. 2013, PASP, 125, 989
Alonso, R., Aigrain, S., Pont, F., Mazeh, T. & CoRoT Exoplanet Science Team 2009, in IAU Symp. 253, Transiting Planets, ed. F. Pont, D. Sasselov, & M. J. Holman (Cambridge, MA: IAU), 91
Anderson, D. R., Hellier, C., Gillon, M., et al. 2010, ApJ, 709, 159
Astropy Collaboration, Robitaille, T. P., Tollerud, E. J., et al. 2013, A&A, 558, A33
Astropy Collaboration, Price-Whelan, A. M., Sipőcz, B. M., et al. 2018, AJ, 156, 123
Bailer-Jones, C. A. L., Rybizki, J., Fouesneau, M., Mantelet, G., & Andrae, R. 2018, AJ, 156, 58
Ballerini, P., Micela, G., Lanza, A. F., & Pagano, I. 2012, A&A, 539, A140
Becker, J. C., Vanderburg, A., Adams, F. C., Rappaport, S. A., & Schwengeler, H. M. 2015, ApJL, 812, L18
Benisty, M., Bae, J., Facchini, S., et al. 2021, ApJL, 916, L2
Berta, Z. K., Charbonneau, D., Bean, J., et al. 2011, ApJ, 736, 12
Bonfanti, A., Delrez, L., Hooton, M. J., et al. 2021, A&A, 646, A157
Borucki, W. J., Koch, D., Basri, G., et al. 2010, Sci, 327, 977
Brown, T. M., Baliber, N., Bianco, F. B., et al. 2013, PASP, 125, 1031
Bryant, E. M., Bayliss, D., Santerne, A., et al. 2021, MNRAS, 504, L45
Buchhave, L. A., Dressing, C. D., Dumusque, X., et al. 2016, AJ, 152, 160
Butler, C. J., Byrne, P. B., Andrews, A. D., & Doyle, J. G. 1981, MNRAS, 197, 815
Cale, B., Plavchan, P., LeBrun, D., et al. 2019, AJ, 158, 170
Cale, B., Reefe, M., Plavchan, P., et al. 2021, AJ, 162, 295
Chambers, J. E. 1999, MNRAS, 304, 793
Chen, J., & Kipping, D. 2017, ApJ, 834, 17
Choi, J., Dotter, A., Conroy, C., et al. 2016, ApJ, 823, 102
Christiansen, J. L., Vanderburg, A., Burt, J., et al. 2017, AJ, 154, 122
Claret, A. 2017, A&A, 600, A30
Claret, A., & Bloemen, S. 2011, A&A, 529, A75
Claret, A., Hauschildt, P. H., & Witte, S. 2012, A&A, 546, A14
Cochran, W. D., Hatzes, A. P., Butler, R. P., & Marcy, G. W. 1997, ApJ, 483, 457
Collins, K. A., Kielkopf, J. F., Stassun, K. G., & Hessman, F. V. 2017, AJ, 153, 77
Cully, S. L., Siegmund, O. H. W., Vedder, P. W., & Vallerga, J. V. 1993, ApJL, 414, L49
Cumming, A., Marcy, G. W., & Butler, R. P. 1999, ApJ, 526, 890
Cutri, R. M., Skrutskie, M. F., van Dyk, S., et al. 2003, VizieR On-line Data Catalog, II/246
Czesla, S., Huber, K. F., Wolter, U., Schröter, S., & Schmitt, J. H. M. M. 2009, A&A, 505, 1277
Czesla, S., Schröter, S., Schneider, C. P., et al. 2019, PyA: Python Astronomy-related packages, Astrophysics Source Code Library, ascl:1906.010
Dalal, S., Kiefer, F., Hébrard, G., et al. 2021, A&A, 651, A11
Davenport, J. R. A., Hawley, S. L., Hebb, L., et al. 2014, ApJ, 797, 122
David, T. J., Petigura, E. A., Luger, R., et al. 2019, ApJL, 885, L12
David, T. J., Hillenbrand, L. A., Petigura, E. A., et al. 2016, Natur, 534, 658
Dawson, R. I., Huang, C. X., Brahm, R., et al. 2021, AJ, 161, 161
Daylan, T., Pinglé, K., Wright, J., et al. 2021, AJ, 161, 85
Deming, D., & Knutson, H. A. 2020, NatAs, 4, 453
Demory, B.-O., Gillon, M., Madhusudhan, N., & Queloz, D. 2016a, MNRAS, 455, 2018
Demory, B.-O., Gillon, M., de Wit, J., et al. 2016b, Natur, 532, 207
Demory, B. O., Pozuelos, F. J., Gómez Maqueo Chew, Y., et al. 2020, A&A, 642, A49
Désert, J.-M., Charbonneau, D., Demory, B.-O., et al. 2011, ApJS, 197, 14
Donati, J. F., Semel, M., Carter, B. D., Rees, D. E., & Collier Cameron, A. 1997, MNRAS, 291, 658
Donati, J. F., Kouach, D., Moutou, C., et al. 2020, MNRAS, 498, 5684
Dotter, A. 2016, ApJS, 222, 8
Ducrot, E., Sestovic, M., Morris, B. M., et al. 2018, AJ, 156, 218
Ducrot, E., Gillon, M., Delrez, L., et al. 2020, A&A, 640, A112
Eastman, J., Siverd, R., & Gaudi, B. S. 2010, PASP, 122, 935
Eastman, J. D., Rodriguez, J. E., Agol, E., et al. 2019, arXiv:1907.09480
Fabrycky, D. C. 2010, arXiv:1006.3834
Fajardo-Acosta, S. B., Beichman, C. A., & Cutri, R. M. 2000, ApJL, 538, L155
Fazio, G. G., Hora, J. L., Allen, L. E., et al. 2004, ApJS, 154, 10
Foreman-Mackey, D. 2018, RNAAS, 2, 31
Foreman-Mackey, D., Agol, E., Ambikasaran, S., & Angus, R. 2017, AJ, 154, 220
Foreman-Mackey, D., Hogg, D. W., Lang, D., & Goodman, J. 2013, PASP, 125, 306
Foreman-Mackey, D., Luger, R., Agol, E., et al. 2021, JOSS, 6, 3285
Gaia Collaboration 2018, VizieR Online Data Catalog, I/345
Gelman, A., & Rubin, D. B. 1992, StaSc, 7, 457
Gilbert, E. A., Barclay, T., Schlieder, J. E., et al. 2020, AJ, 160, 116
Gilbert, E. A., Barclay, T., Quintana, E. V., et al. 2022, AJ, 163, 147
Gillon, M., Demory, B. O., Benneke, B., et al. 2012, A&A, 539, A28
Gillon, M., Jehin, E., Lederer, S. M., et al. 2016, Natur, 533, 221
Gillon, M., Triaud, A. H. M. J., Demory, B.-O., et al. 2017a, Natur, 542, 456
Gillon, M., Demory, B.-O., Van Grootel, V., et al. 2017b, NatAs, 1, 0056

Grillmair, C. J., Charbonneau, D., Burrows, A., et al. 2007, ApJL, 658, L115
Grimm, S. L., Demory, B.-O., Gillon, M., et al. 2018, A&A, 613, A68
Hadden, S., & Lithwick, Y. 2014, ApJ, 787, 80
Haffert, S. Y., Bohn, A. J., de Boer, J., et al. 2019, NatAs, 3, 749
Harris, C. R., Millman, K. J., van der Walt, S. J., et al. 2020, Natur, 585, 357
Hebb, L., Petro, L., Ford, H. C., et al. 2007, MNRAS, 379, 63
Henry, G. W., Marcy, G. W., Butler, R. P., & Vogt, S. S. 2000, ApJL, 529, L41
Holman, M. J., & Murray, N. W. 2005, Sci, 307, 1288
Holt, J. R. 1893, AstAp, 12, 646
Howell, S. B., Sobeck, C., Haas, M., et al. 2014, PASP, 126, 398
Hunter, J. D. 2007, CSE, 9, 90
Ingalls, J. G., Krick, J. E., Carey, S. J., et al. 2012, Proc. SPIE, 8442, 84421Y
Ingalls, J. G., Krick, J. E., Carey, S. J., et al. 2018, Proc. SPIE, 10698, 106985E
Ingalls, J. G., Krick, J. E., Carey, S. J., et al. 2016, AJ, 152, 44
Jenkins, J. M., Twicken, J. D., McCauliff, S., et al. 2016, Proc. SPIE, 9913, 99133E
Jensen, E. 2013, Tapir: A web interface for transit/eclipse observability, Astrophysics Source Code Library, ascl:1306.007
Kalas, P., Liu, M. C., & Matthews, B. C. 2004, Sci, 303, 1990
Keppler, M., Benisty, M., Müller, A., et al. 2018, A&A, 617, A44
Klein, B., Donati, J.-F., Moutou, C., et al. 2021, MNRAS, 502, 188
Kostov, V. B., Orosz, J. A., Feinstein, A. D., et al. 2020, AJ, 159, 253
Kreidberg, L. 2015, PASP, 127, 1161
Kundu, M. R., Jackson, P. D., White, S. M., & Melozzi, M. 1987, ApJ, 312, 822
Lagrange, A. M., Gratadour, D., Chauvin, G., et al. 2009, A&A, 493, L21
Lagrange, A. M., Meunier, N., Rubini, P., et al. 2019, NatAs, 3, 1135
Lam, K. W. F., Korth, J., Masuda, K., et al. 2020, AJ, 159, 120
Lannier, J., Lagrange, A. M., Bonavita, M., et al. 2017, A&A, 603, A54
Lanotte, A. A., Gillon, M., Demory, B. O., et al. 2014, A&A, 572, A73
Laskar, J. 1997, A&A, 317, L75
Laskar, J. 2000, PhRvL, 84, 3240
Laskar, J., & Petit, A. C. 2017, A&A, 605, A72
Leleu, A., Alibert, Y., Hara, N. C., et al. 2021, A&A, 649, A26
Lewis, N. K., Knutson, H. A., Showman, A. P., et al. 2013, ApJ, 766, 95
Lightkurve Collaboration, Cardoso, J. V. d. M., Hedges, C., et al. 2018, Lightkurve: Kepler and TESS time series analysis in Python, Astrophysics Source Code Library, ascl:1812.013
Lithwick, Y., Xie, J., & Wu, Y. 2012, ApJ, 761, 122
Liu, M. C., Matthews, B. C., Williams, J. P., & Kalas, P. G. 2004, ApJ, 608, 526
Mahtani, D. P., Maxted, P. F. L., Anderson, D. R., et al. 2013, MNRAS, 432, 693
Mamajek, E. E., & Bell, C. P. M. 2014, MNRAS, 445, 2169
Mandel, K., & Agol, E. 2002, ApJL, 580, L171
Mann, A. W., Gaidos, E., Mace, G. N., et al. 2016, ApJ, 818, 46
Mannaday, V. K., Thakur, P., Jiang, I.-G., et al. 2020, AJ, 160, 47
Marois, C., Macintosh, B., Barman, T., et al. 2008, Sci, 322, 1348
Marois, C., Zuckerman, B., Konopacky, Q. M., Macintosh, B., & Barman, T. 2010, Natur, 468, 1080
Martioli, E. 2020, private communication
Martioli, E., Hébrard, G., Correia, A. C. M., Laskar, J., & Lecavelier des Etangs, A. 2021, A&A, 649, A177
Martioli, E., Hébrard, G., Moutou, C., et al. 2020, A&A, 641, L1
Mayor, M., & Queloz, D. 1995, Natur, 378, 355
Mazeh, T., Nachmani, G., Holczer, T., et al. 2013, ApJS, 208, 16
McLaughlin, D. B. 1924, ApJ, 60, 22
Mendonça, J. M., Malik, M., Demory, B.-O., & Heng, K. 2018, AJ, 155, 150
Morin, J., Donati, J. F., Petit, P., et al. 2010, MNRAS, 407, 2269
Morris, B. 2020, JOSS, 5, 2103
Morris, B. M., Agol, E., Hebb, L., et al. 2018, ApJL, 863, L32
Moutou, C., Dalal, S., Donati, J. F., et al. 2020, A&A, 642, A72
Newton, E. R., Mann, A. W., Tofflemire, B. M., et al. 2019, ApJL, 880, L17
Ohta, Y., Taruya, A., & Suto, Y. 2005, ApJ, 622, 1118
Osborn, A., Armstrong, D. J., Cale, B., et al. 2021, MNRAS, 507, 2782
Oshagh, M., Boué, G., Haghighipour, N., et al. 2012, A&A, 540, A62
Oshagh, M., Santos, N. C., Boisse, I., et al. 2013, A&A, 556, A19
Pallé, E. 2020, private communication
Palle, E., Oshagh, M., Casasayas-Barris, N., et al. 2020, A&A, 643, A25
Pepe, F., Cristiani, S., Rebolo, R., et al. 2021, A&A, 645, A96
Pérez, F., & Granger, B. E. 2007, CSE, 9, 21
Pitkin, M., Williams, D., Fletcher, L., & Grant, S. D. T. 2014, MNRAS, 445, 2268
Plavchan, P., Jura, M., & Lipscy, S. J. 2005, ApJ, 631, 1161
Plavchan, P., Werner, M. W., Chen, C. H., et al. 2009, ApJ, 698, 1068
Plavchan, P., Barclay, T., Gagné, J., et al. 2020, Natur, 582, 497
Pont, F., Gilliland, R. L., Moutou, C., et al. 2007, A&A, 476, 1347
Rainer, M., Borsa, F., Pino, L., et al. 2021, A&A, 649, A29
Rayner, J., Tokunaga, A., Jaffe, D., et al. 2016, Proc. SPIE, 9908, 990884
Rein, H., & Liu, S. F. 2012, A&A, 537, A128
Rein, H., & Spiegel, D. S. 2015, MNRAS, 446, 1424
Ricker, G. R., Winn, J. N., Vanderspek, R., et al. 2015, JATIS, 1, 014003
Rodriguez, J. E., Quinn, S. N., Zhou, G., et al. 2021, AJ, 161, 194
Rosenthal, L. J., Fulton, B. J., Hirsch, L. A., et al. 2021, ApJS, 255, 8
Rossiter, R. A. 1924, ApJ, 60, 15
Sanchis-Ojeda, R., & Winn, J. N. 2011, ApJ, 743, 61
Sanchis-Ojeda, R., Winn, J. N., Holman, M. J., et al. 2011, ApJ, 733, 127
Sato, B., Wang, L., Liu, Y.-J., et al. 2016, ApJ, 819, 59
Smith, J. C., Stumpe, M. C., Van Cleve, J. E., et al. 2012, PASP, 124, 1000
Song, I., Weinberger, A. J., Becklin, E. E., Zuckerman, B., & Chen, C. 2002, AJ, 124, 514
Stangret, M., Pallé, E., Casasayas-Barris, N., et al. 2021, A&A, 654, A73
Stauffer, J., Tanner, A. M., Bryden, G., et al. 2010, PASP, 122, 885
Stevenson, K. B., Harrington, J., Fortney, J. J., et al. 2012, ApJ, 754, 136
Stumpe, M. C., Smith, J. C., Catanzarite, J. H., et al. 2014, PASP, 126, 100
Stumpe, M. C., Smith, J. C., Van Cleve, J. E., et al. 2012, PASP, 124, 985
Sun, L., Ioannidis, P., Gu, S., et al. 2019, A&A, 624, A15
Szabó, G. M., Gandolfi, D., Brandeker, A., et al. 2021, A&A, 654, A159
Todorov, K. O., Deming, D., Burrows, A., & Grillmair, C. J. 2014, ApJ, 796, 100
Triaud, A. H. M. J. 2018, The Rossiter–McLaughlin Effect in Exoplanet Research (Berlin: Springer), 2
Triaud, A. H. M. J., Queloz, D., Bouchy, F., et al. 2009, A&A, 506, 377
Trifonov, T. 2019, The Exo-Striker: Transit and radial velocity interactive fitting tool for orbital analysis and N-body simulations, Astrophysics Source Code Library, ascl:1906.004
Tsikoudi, V., & Kellett, B. J. 2000, MNRAS, 319, 1147
Virtanen, P., Gommers, R., Oliphant, T. E., et al. 2020, NatMe, 17, 261
Wang, S., Winn, J. N., Addison, B. C., et al. 2021, AJ, 162, 50
Werner, M. W., Roellig, T. L., Low, F. J., et al. 2004, ApJS, 154, 1
White, R., Schaefer, G., Boyajian, T., et al. 2019, AAS Meeting Abstracts, 233, 259.41
Winn, J. N. 2007, in ASP Conf. Ser. 366, Transiting Extrapolar Planets Workshop, ed. C. Afonso, D. Weldrake, & T. Henning (San Francisco, CA: ASP), 170
Zacharias, N., Finch, C. T., Girard, T. M., et al. 2012, VizieR Online Data Catalog, I/322A
Zechmeister, M., Reiners, A., Amado, P. J., et al. 2018, A&A, 609, A12
Zellem, R. T., Lewis, N. K., Knutson, H. A., et al. 2014, ApJ, 790, 53
Zhang, Z., Zhou, Y., Rackham, B. V., & Apai, D. 2018, AJ, 156, 178
Zuckerman, B. 2001, ARA&A, 39, 549